Effects of Alexander disease–associated mutations on the assembly and organization of GFAP intermediate filaments

Ai-Wen Yang[a,†], Ni-Hsuan Lin[a,†], Ting-Hung Yeh[b], Natasha Snider[c], and Ming-Der Perng[a,b,*]
[a]Institute of Molecular Medicine and [b]Department of Medical Science, College of Life Sciences, National Tsing Hua University, Hsinchu 30013, Taiwan; [c]Department of Cell Biology and Physiology, University of North Carolina at Chapel Hill, Chapel Hill, NC 27599

ABSTRACT **Alexander disease is a primary genetic disorder of astrocytes caused by dominant mutations in the gene encoding glial fibrillary acidic protein (GFAP). How single-amino-acid changes can lead to cytoskeletal catastrophe and brain degeneration remains poorly understood. In this study, we have analyzed 14 missense mutations located in the GFAP rod domain to investigate how these mutations affect in vitro filament assembly. Whereas the internal rod mutants assembled into filaments that were shorter than those of wild type, the rod end mutants formed structures with one or more of several atypical characteristics, including short filament length, irregular width, roughness of filament surface, and filament aggregation. When transduced into primary astrocytes, GFAP mutants with in vitro assembly defects usually formed cytoplasmic aggregates, which were more resistant to biochemical extraction. The resistance of GFAP to solubilization was also observed in brain tissues of patients with Alexander disease, in which a significant proportion of insoluble GFAP were accumulated in Rosenthal fiber fractions. These findings provide clinically relevant evidence that link GFAP assembly defects to disease pathology at the tissue level and suggest that altered filament assembly and properties as a result of GFAP mutation are critical initiating factors for the pathogenesis of Alexander disease.**

Monitoring Editor
Thomas Magin
University of Leipzig

Received: Jan 18, 2022
Revised: Mar 30, 2022
Accepted: Apr 25, 2022

INTRODUCTION

Alexander disease (AxD) is a rare and often fatal neurological disease that often affects the white matter of the CNS. Based on the age of onset, the clinical signs and progression of AxD are highly variable (Prust *et al.*, 2011). The early-onset form is more common, with an onset during the first 2 yr of life. This form is often associated with a rapid disease progression and characterized by the loss of myelin and dramatic changes in white matter. Typically, patients exhibit symptoms including developmental delays, megalencephaly, abnormal myelination, and seizures. The late-onset form, which occurs at any age, tends to display bulbar and pseudobulbar signs such as excessive vomiting, difficulty swallowing and speaking, poor coordination, and loss of motor control. A prominent neuropathological feature of both forms of AxD is the abundant presence of Rosenthal fibers (RFs) in the subpial, perivascular, and subventricular regions of the brain. RFs are astrocytic inclusions of protein complex containing vimentin, ubiquitin, plectin (Tian *et al.*, 2006), αB-crystallin (Goldman and Corbin, 1991; Heaven *et al.*, 2016), p62 (Zatloukal *et al.*, 2002), and the recently described cyclin D2 (Heaven *et al.*, 2016) and glial fibrillary acidic protein (GFAP) minor isoforms including GFAP-δ and GFAP-λ (Lin *et al.*, 2021). Although RFs is a pathological hallmark associated with AxD, their causality in its pathogenesis is not yet clear.

Genetically, mutations in GFAP are found in more than 95% of patients clinically diagnosed with AxD, and there are now more than 100 such mutations causally associated with this disease (Messing and Brenner, 2020). Most of these mutations are typically missense nucleotide changes predicting single-amino-acid substitutions

This article was published online ahead of print in MBoC in Press (http://www.molbiolcell.org/cgi/doi/10.1091/mbc.E22-01-0013) on May 5, 2022.
Conflict of interest: There are no conflicts of interest in connection with this article.
[†]These authors contributed equally to this work.
*Address correspondence to: Ming-Der Perng (mdperng@life.nthu.edu.tw).
Abbreviations used: AxD, Alexander disease; GFAP, glial fibrillary acidic protein; IF, intermediate filament; RF, Rosenthal fiber; ULF, unit length filament; WT, wild type.

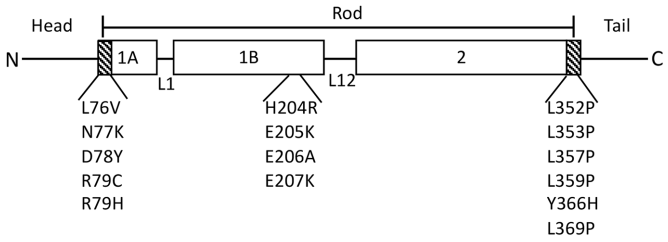

FIGURE 1: Location of GFAP mutations relative to its secondary structure. Like all IF proteins, the GFAP is fibrous in nature and exhibits a tripartite structure with a central α-helical coiled-coil domain ("rod") flanked by non–α-helical "head" and "tail" domains. (denoted by black bars). Within the rod, three coil-forming segments (coil 1A, 1B, and 2 denoted by boxes) are separated by short linker sequences (L1 and L12). Hatched boxes denote the highly conserved IF consensus motifs at both ends of the rod domain. The GFAP mutations investigated in this study are given beneath the diagram.

spread throughout the entire sequence of GFAP. Almost all mutations detected so far are heterozygous coding mutations, which are genetically dominant and therefore are expected to act in a gain-of-function manner. In approximately one-third of all published studies, patients have mutations at just four amino acids, R79, R88, R239, and R416, which are highly homologous to hot spots for mutations in other intermediate filaments (IFs) (Brenner *et al.*, 2008). With the exception of the R239H mutation that has been identified in many early-onset patients, genotype and phenotype correlations are not apparent for most of the GFAP mutations.

Like other IF proteins, GFAP has a characteristic domain structure comprising a central α-helical rod domain flanked by non–α-helical N-terminal head and C-terminal tail domains. With the exception of a few missense mutations residing in either the head or the tail domain, most pathogenic GFAP mutations discovered to date are located in the rod domain. The highly conserved LNDR and TYRKLEGGE motifs are present at the start and end of this rod domain, and those mutations found within them are usually associated with the most severe forms of AxD. As yet, the impact of these GFAP mutations on the process of filament assembly is only poorly understood. Given that mutations all along the length of GFAP result in AxD and yield similarly appearing protein aggregates, it has been assumed that there is a common assembly defect that generally interfere with normal filament assembly. This notion has prevailed to such an extent that it had never been tested experimentally.

In this study, we have performed a systematic analysis of 14 missense mutations located in different regions of the GFAP rod domain to investigate how these mutations affect filament assembly in vitro and network formation in primary astrocytes. To investigate the link that connects GFAP assembly defects to disease pathology at the tissue level, we test whether mutant GFAPs formed RFs in the brain tissues of human AxD patients.

RESULTS

Effects of rod end mutations upon in vitro assembly

To understand how AxD-associated mutations may affect the filament assembly process, we first focused on GFAP mutations located at the LNDR motif, spanning amino acids 76 and 79 in coil 1A of the rod domain (Figure 1). Purified recombinant wild-type (WT) and mutant GFAPs were assembled in vitro by stepwise dialysis, followed by negative staining and electron microscopy. While WT GFAP assembled into typical 10-nm filaments that were several microns in length and uniform in width (Figure 2A), all the LNDR mutations perturbed in vitro filament assembly. The L76V mutant assembled into filaments that exhibited atypical structures, including short filament length, irregular width, and roughness of filament surface (Figure 2B). In contrast, the N77K GFAP failed to assemble into 10-nm filaments but formed structures that were variable in length and irregular in width (Figure 2C, arrows), some of which were interconnected end to end forming abnormal structures that were never seen in WT filaments. Similarly, filaments formed by the D78Y GFAP were significantly shorter, as evidenced by an increase in the number of free filament ends seen in the electron micrograph (Supplemental Figure S1A). The most aberrant filaments were those assembled from R79C (Supplemental Figure S1B) and R79H (Figure 2D) GFAP mutants, which formed short rod-like structures of irregular diameter that looked like short filament pieces and failed to elongate and compact properly into 10-nm filaments (Figure 2D, arrows).

To mimic the heterozygous situation in AxD patients where WT and mutant proteins are coexpressed, we carried out coassembly experiments. When R79H and WT GFAP were coassembled in a 10:90 ratio (Supplemental Figure S1C), the filaments formed were not dramatically different from those of WT alone. Increasing the proportion of R79C GFAP to 25% in the assembly mixture, however, resulted in filaments that were irregular in diameter (Figure 2E, arrows and arrowheads). At a 50:50 proportion of WT and R79C GFAP, filament assembly was disrupted and short filament pieces with irregular width were formed (Figure 2F). These data suggest that the effect of the R79H GFAP mutant is dominant over the WT protein with respect to in vitro filament assembly.

Filament organization and solubility properties of GFAP rod end mutants

To investigate the effects of GFAP mutations on the formation of IF networks, WT and mutant GFAPs were transduced by lentiviral infection into primary astrocytes in which GFAP is naturally expressed. To track the expression of GFAPs, transduced astrocytes were immunostained with an anti-GFAP antibody that preferentially recognized human GFAP (Lin *et al.*, 2017). Whereas WT GFAP mainly integrated into filamentous networks with the endogenous GFAP (Figure 3A), the R79H mutant formed large aggregates (Figure 3B) composed of small ring-like structures scattered throughout the cytoplasm (Figure 3B, arrows). Similar GFAP-enriched aggregates were also observed in astrocytes transduced with L76V, N77K, D78Y, and R79C mutant GFAPs (Supplemental Figure S1, D–G), which collapsed the endogenous IF networks in >90% of transduced cells. In mutant GFAP–transduced cells. the small heat shock protein αB-crystallin (Figure 3D, arrows) was seen colocalized with a proportion of densely stained GFAP aggregates. This is in contrast to astrocytes transduced with WT GFAP, in which the αB-crystallin was distributed throughout the cytoplasm (Figure 3C).

To test whether cytoplasmic aggregates formed in GFAP mutant–expressing astrocytes had solubility properties different from those of WT, transduced cells were extracted using a extraction protocol that solubilized nonaggregated forms of GFAP but retained GFAP aggregates (Lin *et al.*, 2021). Analysis of the supernatant (Figure 3E) and pellet (Figure 3F) fractions by immunoblotting revealed that whereas WT GFAP was almost completely extracted from WT GFAP–transduced cells (Figure 3E, lane 2), all the GFAP mutants, except for the D78Y GFAP (Figure 3F, lane 5), were more resistant to extraction and remained mainly in the pellet fraction (Figure 3F, lanes 3, 4, and 6). Because cells transduced with either WT or mutant GFAP generated stable proteins of the expected size at roughly comparable levels (Figure 3G, lanes 2–6), aggregate

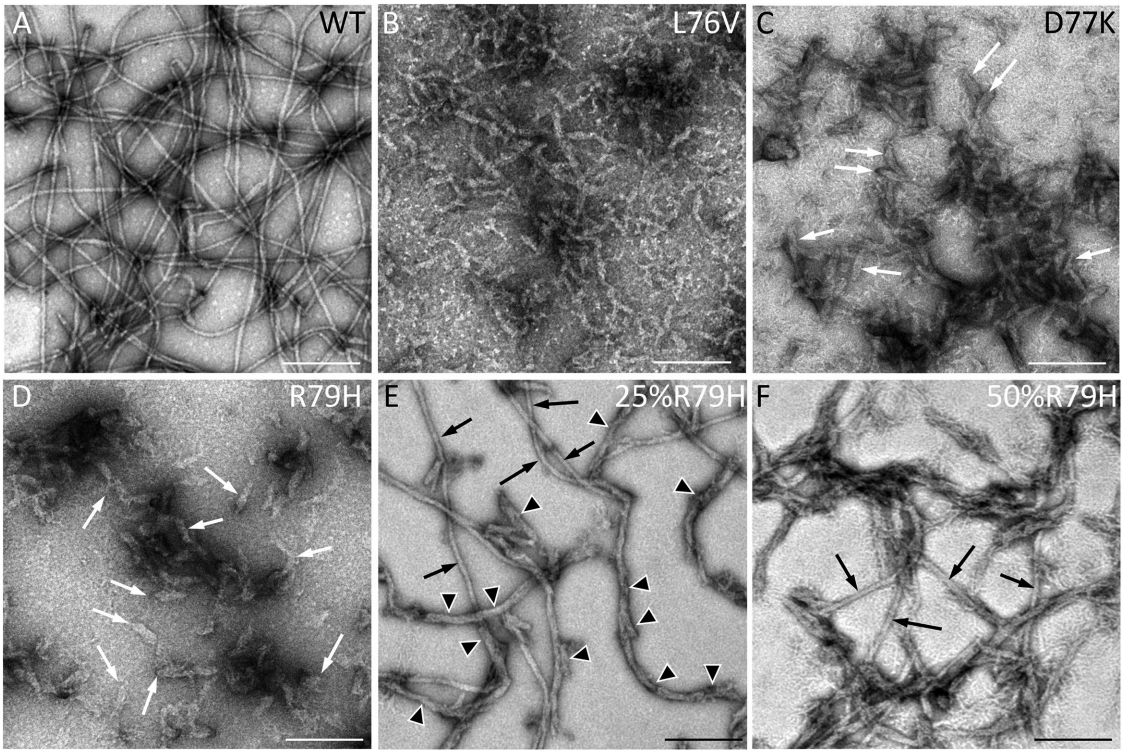

FIGURE 2: Electron micrographs of in vitro assembly structures generated by WT and mutant GFAPs. Purified recombinant WT (A) and mutant (B–D) GFAPs assembled in vitro were negatively stained and visualized by transmission electron microscopy. Under these assembly conditions, WT GFAP assembled into typical 10-nm filaments with length of several microns (A), whereas N76V (B) formed only short filament pieces with unraveled structures. Both L77K (C) and R79H (D) GFAP formed mainly ULFs that failed to elongate (indicated by white arrows). When WT and R79H were coassembled at a 75:25 proportion, filaments with uneven width were clearly seen (E). In E, arrows indicate normal-diameter filament segments; arrowheads point to unusually thick, compacted filaments. Coassembly of WT GFAP in a 50:50 proportion with R79H GFAP disrupted the normal assembly of WT GFAP (F), producing only short and unraveled structures with few normal filaments with WT morphology (F, black arrows). Bar, 200 nm.

formation is likely due to the mutation per se rather than elevated expression levels. Notably, the accumulation of GFAP aggregates in astrocytes transduced with mutant GFAPs also correlated with the detection of elevated levels of the small stress proteins αB-crystallin and high-molecular-weight ubiquitinated proteins in the pellet fraction (Figure 3F, lanes 3, 4, and 6).

We next examined whether mutations near the highly conserved segment of the rod end, including the IF consensus motif TYRKLEGGE, might also perturb the structure of GFAP in a manner deleterious to its assembly. Under standard in vitro assembly conditions, none of the rod end mutants formed filaments exhibiting WT regularity in width, length, and surface smoothness. Both L352P (Supplemental Figure S2A) and L353P (Figure 4A) GFAP formed large, irregularly shaped aggregates from which abnormal filaments with irregular width occasionally protruded (Figure 4A, arrows). In contrast, the L357P GFAP (Figure 4B) failed to assemble into filament. Some of the unpolymerized materials appeared to resemble structures with dimensions of a unit length filament (ULF), which were 63.2 ± 8.7 nm long and variable in width (Figure 4B, arrows). Filaments formed from the L359P mutant were not as long or as uniform as WT filaments, and many were less than 100 nm in length (Supplemental Figure S2B). Unpolymerized materials in the background were frequently seen, indicative that assembly was not as efficient as in WT. Although the L369P GFAP was able to form filament-like structures, they were irregular in width and some exhibited roughness with small protuberances along the filament surface (Supplemental Figure S2C). The Y366H GFAP was unusual in its inability to assemble into extended filaments (Figure 4C) but formed short rod-like filament pieces (Figure 4C, inset) that had a strong tendency to laterally associate into aggregates. Coassembly titrations showed that even the 10% Y366H mutant in the coassembly mixture altered the morphology of the WT filaments, which appeared more irregular in width and partially unraveled (Figure 4D, arrowheads). With increasing Y366H GFAP to 25% in the assembly mixture, more filament disruption was observed (Figure 4E, arrows and arrowheads). At a 50:50 proportion, typical 10-nm filaments were not seen, but aggregates similar to those made by the Y366H mutant alone were formed instead (Supplemental Figure S2D). These data show that the Y366H GFAP mutant failed to longitudinally anneal and formed mainly UFL-like structures that aggregated strongly and that this effect is again dominant over the WT protein.

These data also suggest that the assembled Y366H GFAP filaments were prone to aggregation. To monitor the extent of filament aggregation in the whole assembly population, we performed a low-speed sedimentation assay (Pollard and Cooper, 1982). With this assay, most (>90%) of the WT GFAP was found in the supernatant fraction (Figure 4F, lane 1). In contrast, Y366H GFAP sedimented more efficiently, with 63 ± 4% of proteins being found in the pellet fraction (Figure 4F, lane 10). Similar sedimentation behaviors were also observed for L352P (Figure 4F, lane 4) and L353P (Figure 4F, lane 6), confirming their aggregation-prone properties. A high-speed sedimentation assay confirmed that WT GFAP had

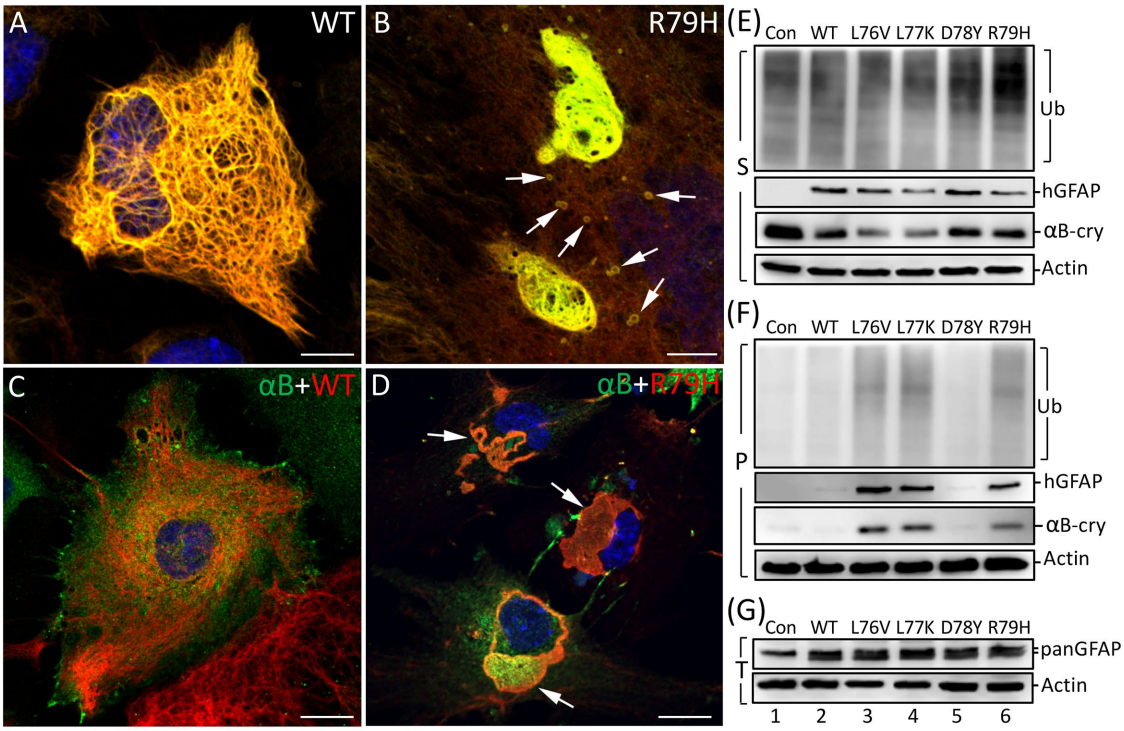

FIGURE 3: Filament organization and solubility properties of WT and mutant GFAP in primary astrocytes. Primary astrocytes were transduced with either WT (A) or R79H mutant (B) GFAP. At 72 h after transduction, cells were processed for double-label immunofluorescence microscopy using a monoclonal anti-GFAP antibody that recognized transduced human GFAP (hGFAP, green channel) and anti-panGFAP antibodies that recognized both the endogenous rat GFAP and transduced hGFAP (red channel). Astrocytes transduced with WT (C) or R79H (D) GFAP were also costained with anti-GFAP (red channel) and anti–αB-crystallin (green channel) antibodies. Nuclei were visualized by staining with DAPI (blue channel). Merged images are shown. Bar, 10 μm. Note that the R79H mutant formed cytoplasmic inclusions with unusual ring-like structures at the cell periphery (B, arrows). (E–G) Solubility properties of WT and mutant GFAPs. Astrocytes transduced with the indicated GFAP constructs were extracted at 72 h posttransduction. The resulting supernatant (E) and pellet (F) fractions were analyzed by immunoblotting using antibodies specific to ubiquitin, hGFAP, and αB-crystallin. Total cell lysates were analyzed by probing with the anti-panGFAP antibody (G). Sample loading amounts were 2.87 μg of protein per lane for the supernatant (E), 2.49 μg of protein per lane for the pellet (F), and 5.4 μg of protein per lane for the total (G). Actin was used as a sample loading control.

assembled efficiently (Figure 4G, lane 2), as evidenced by >90% of the protein being pelleted under conditions known to sediment polymerized GFAP filaments (Nicholl and Quinlan, 1994). Under these centrifugation conditions, all the GFAP mutants also sedimented into the pellet fraction (Figure 4G, lanes 4, 6, and 10), but this was not the case for the L357P GFAP. A sizable proportion (~65%) of this mutant remained soluble (Figure 4G, lane 7), consistent with the results of electron microscopy that this mutant failed to assemble into filaments (Figure 4B).

When transduced into primary astrocytes for 72 h, the GFAP C-terminal rod end mutants all failed to form filamentous networks. The Y366H mutant (Figure 4H) formed large aggregates with small clumps at the cell periphery (Figure 4H, arrows) in >90% of transduced cells. Similar aggregates were observed when astrocytes were transduced with L352P, L353P, L357P, L359P, and L369P mutant GFAPs (Supplemental Figure S2, E–I). The number of cells containing GFAP aggregates and the extent of aggregation did not change appreciably when cells were transduced for 24 h (Supplemental Figure S3, A–F) and 48 h (Supplemental Figure S3, G–L). The GFAP aggregates still formed when the mutant GFAPs were cotransduced with WT GFAP in a 1:1 ratio (Supplemental Figure S4), consistent with the dominant effect of these mutations.

To assess biochemically the solubility properties of the mutant GFAPs, primary astrocytes transduced with either WT or mutant GFAPs were extracted and the resulting supernatant and pellet fractions were analyzed by immunoblotting. Whereas WT GFAP was extracted completely from WT GFAP–transduced astrocytes (Figure 3E, lane 2), all C-terminal rod end mutants were more resistant to extraction, with most of the mutant GFAPs remaining in the pellet fraction (Figure 4I, lanes 1–6). Analysis of the total cell lysates of transduced cells revealed that GFAPs levels were increased at comparable levels (Supplemental Figure S2J, lanes 1–6). Levels of αB-crystallin (Figure 4I, lanes 1–6) and high-molecular-weight ubiquitinated proteins (Supplemental Figure S2J, lanes 1–6) were also increased in the pellet fraction of mutant GFAP–transduced cells compared with WT controls (Figure 3F, lane 2). These changes correlated with the detection of a GFAP proteolytic fragment (p26) in the pellet fraction of mutant GFAP–transduced cells (Figure 4I, lanes 1, 4, and 5), which most likely reflected caspase-generated cleavage product (Chen *et al.*, 2013).

To evaluate the potential effects of GFAP-containing aggregates on astrocyte function, membrane fractions prepared from untransduced controls (Figure 4J, lane 1) or GFAP-transduced astrocytes (Figure 4J, lanes 2–4) were analyzed by immunoblotting. Astrocytes transduced with mutant GFAP exhibited a significant reduction in expressions of the glutamate transporter Glt-1 and gap junction protein connexin 43 (Figure 4J, lanes 3 and 4) compared with those transduced with WT GFAP (Figure 4J, lane 2) and untransduced

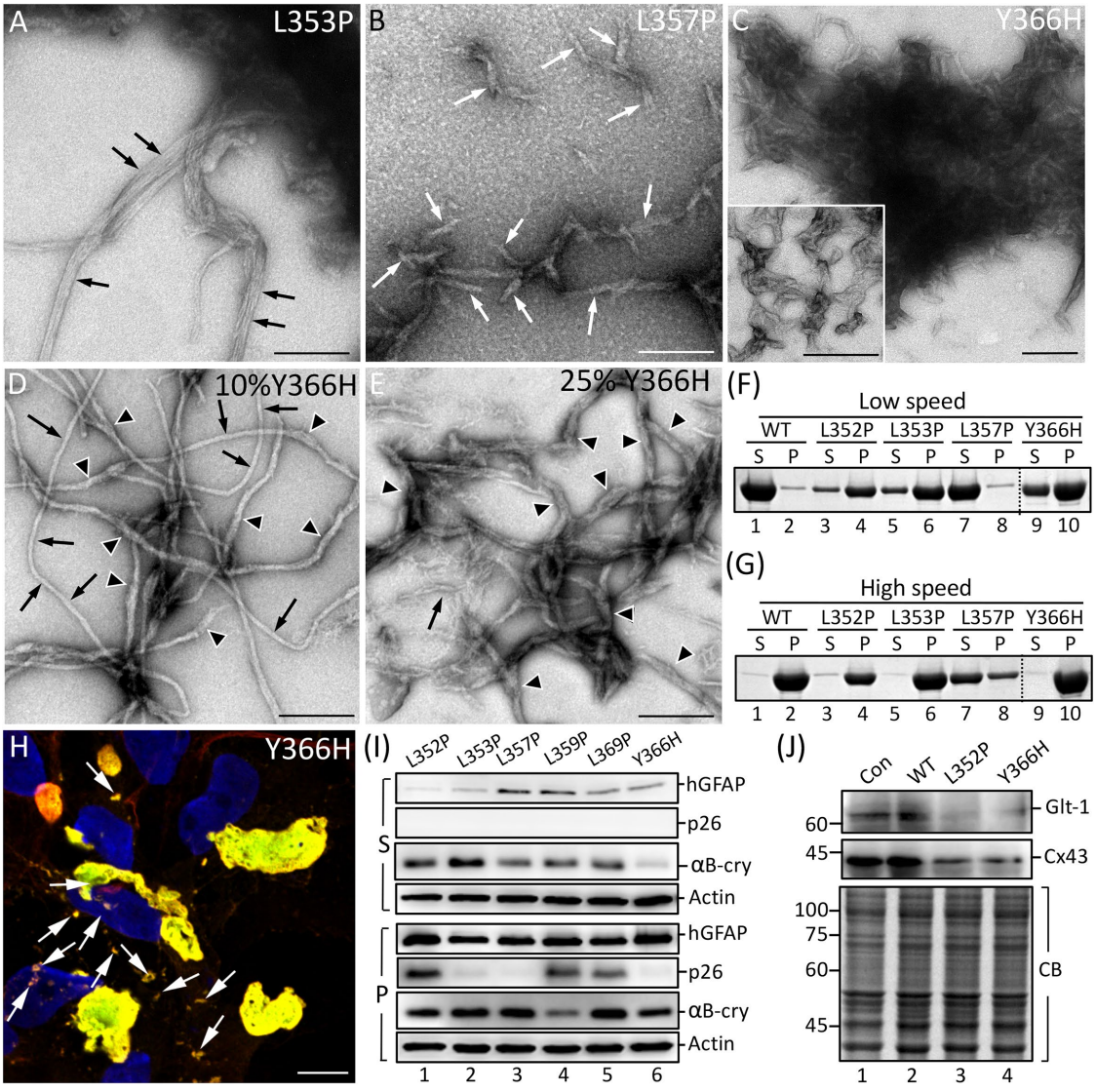

FIGURE 4: Assembly properties of GFAP variants with mutations located at the C-terminal end of GFAP coil 2. (A–C). Purified recombinant mutant GFAPs were assembled in vitro and visualized by electron microscopy. In A, arrows highlight possible lateral fusion events leading to thick filaments formed by the L353P GFAP. Note that in this micrograph, sampling was restricted to regions of the electron microscopic grid in which individual filaments can be seen. Whereas L357P GFAP assembled into ULF-like structures that failed to elongate (B, arrows), the Y366H mutant alone formed short filaments that had a strong tendency to aggregate (C). In less-aggregated areas and at a higher magnification, the filamentous-like structures that comprise the aggregates are clearly seen (C, inset). (D, E) WT and Y366H GFAP were coassembled in mixtures of the indicated proportions. In D, arrows indicate segments of filaments with normal diameter probably originating from WT GFAP; arrowheads indicate abnormal filaments with enlarged diameter. In E, arrowheads indicate thick filament segments obviously originating from the Y366H mutant; arrows indicate short filament pieces with unraveled structures. Bar, 200 nm. (F, G) Assembled WT (lanes 1 and 2) and mutant (lanes 3–10) GFAPs were subjected to low-speed (F) and high-speed (G) centrifugations as described in *Materials and Methods*. After centrifugation, the supernatant (S) and pellet (P) fractions were analyzed by SDS–PAGE and visualized by Coomassie blue staining. Representative gels are shown, and the mutant GFAPs analyzed by these assays are indicated above the gels. Dash lines indicate lanes that separate samples run on different gels. (H) Effect of Y366H GFAP mutants upon IF network formation was visualized by immunostaining with anti-hGFAP (green channel) and anti-panGFAP (red channel) antibodies. Bar, 10 μm. (I) Solubility properties of mutant GFAPs. Primary astrocytes transduced with the indicated GFAP constructs were extracted, and the supernatant (S) and pellet (P) fractions were analyzed by immunoblotting using the indicated antibodies. Actin was used as a sample loading control. Note that a GFAP degradation product (p26) was detected in some but not all mutant GFAP–transduced cells (I, lanes 1, 4, and 5). (J) Membrane-enriched fractions (32 μg of protein loading per lane) prepared from either untransduced astrocytes (lane 1) or astrocytes transduced with the indicated GFAPs (lanes 2–4) were analyzed by immunoblotting with antibodies to glutamate transporter-1 (Glt-1) and connexin 43 (Cx43). A duplicate gel stained with Coomassie blue (CB) is shown to assist comparison of equal protein loading.

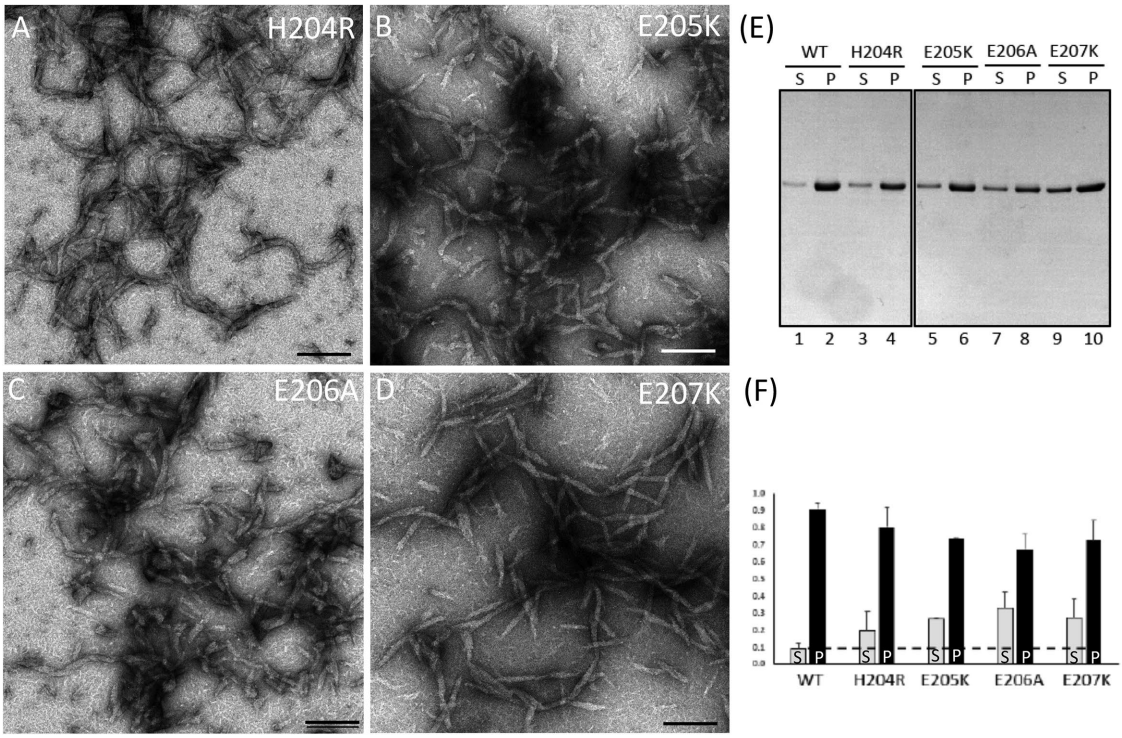

FIGURE 5: Effects of the internal rod GFAP mutants upon filament assembly in vitro. Purified recombinant GFAP mutants (A–D) were assembled in vitro and visualized by negative staining followed by electron microscopy. Scale bar represents 200 nm. Assembled GFAP mutants were subjected to a high-speed centrifugation, and the supernatant (S) and pellet (P) fractions were analyzed by SDS–PAGE and visualized by Coomassie blue staining (E). Quantification results from three independent experiments are shown as mean ± SE and represented as bar charts (F).

controls (Figure 4J, lane 1). These data suggest that aggregates of mutant GFAPs may also impact astrocyte functions.

Effects of the GFAP coil 2 fragment on IF assembly

These results also suggest that the precise sequence of the C-terminal rod end is critical for GFAP assembly. Therefore we performed a cosedimentation assay to investigate whether the coil 2 fragment, encompassing amino acids 257–370 of human GFAP, affects filament assembly by interacting with GFAP. Whereas most of the WT GFAP sedimented into the pellet fraction (Supplemental Figure S5A, lane 2), the coil 2 fragment remained almost entirely in the supernatant fraction (Supplemental Figure S5A, lane 7). Coassembly of GFAP in a 1:1 molar ratio with the coil 2 fragment resulted in a sizable proportion of this fragment cosedimented with GFAP into the pellet fraction (Supplemental Figure S5A, lane 4). When mixed with preassembled GFAP filaments in a 1:1 ratio, most of the coil 2 fragment was found to cosediment with GFAP filaments (Supplemental Figure S5A, lane 6). These changes in the sedimentation behavior suggest an interaction of the coil 2 fragment with GFAP. To visualize this interaction, samples were negatively stained, followed by electron microscopy. Whereas WT GFAP formed typical 10-nm filaments (Supplemental Figure S5B), coassembly of the coil 2 fragment with GFAP resulted in the formation of short filamentous intermediates that had a strong tendency to aggregate (Supplemental Figure S5C). Mixing the coil 2 fragment with preassembled GFAP led to a dramatic disassembly of GFAP filament into short and irregular fibrillar structures (Supplemental Figure S5D). These data show that the coil 2 fragment inhibits filament assembly and disassembles preformed filaments by interacting with GFAP.

Internal rod GFAP mutations perturb filament assembly and formation

Having already demonstrated that mutations at both ends of the rod domain had a potent effect on GFAP assembly and IF network formation, we wondered whether mutations located more central to the rod domain might also perturb the α-helical rod in a manner that affects filament assembly. To test the effects of the GFAP internal rod mutations, we introduced nucleotide changes encoding H204R, E205K, E206A, and E207K mutations in the coil 1B of the rod domain (Figure 1). Whereas WT GFAP assembled into long and smooth filaments (Figure 2A), all four internal rod mutations perturbed GFAP assembly in vitro (Figure 5, A–D). The H204R mutant GFAP produced comparatively shorter and less uniform filaments, even after prolonged assembly (Figure 5A). This feature was particularly prominent for E205K (Figure 5B) and E206A (Figure 5C), which made filaments with an average length of only 100–200 nm and with no filaments appreciably longer than this. The E207K mutant GFAP formed significantly short filaments that were more angular, more irregular in width, and partially unraveled (Figure 5D). A high-speed sedimentation assay confirmed that all internal rod mutants assembled less efficiently than WT GFAP (Figure 5E), as a significant proportion of mutant proteins were found in the supernatant fraction (Figure 5F).

When transduced into astrocytes, E205K (Figure 6B), E206A (Supplemental Figure S6A), and E207K (Supplemental Figure S6B) mutant GFAPs formed aggregates in 21, 24, and 29% of transduced cells, respectively. In contrast, the H204R mutant GFAP (Figure 6A) generated IF networks that were indistinguishable from those made by WT GFAP (Figure 3A). Biochemical fractionation showed that GFAP levels were increased in the pellet fraction of astrocytes transduced with E205K (Figure 6C, lane 4), E206A (Figure 6C, lane 5),

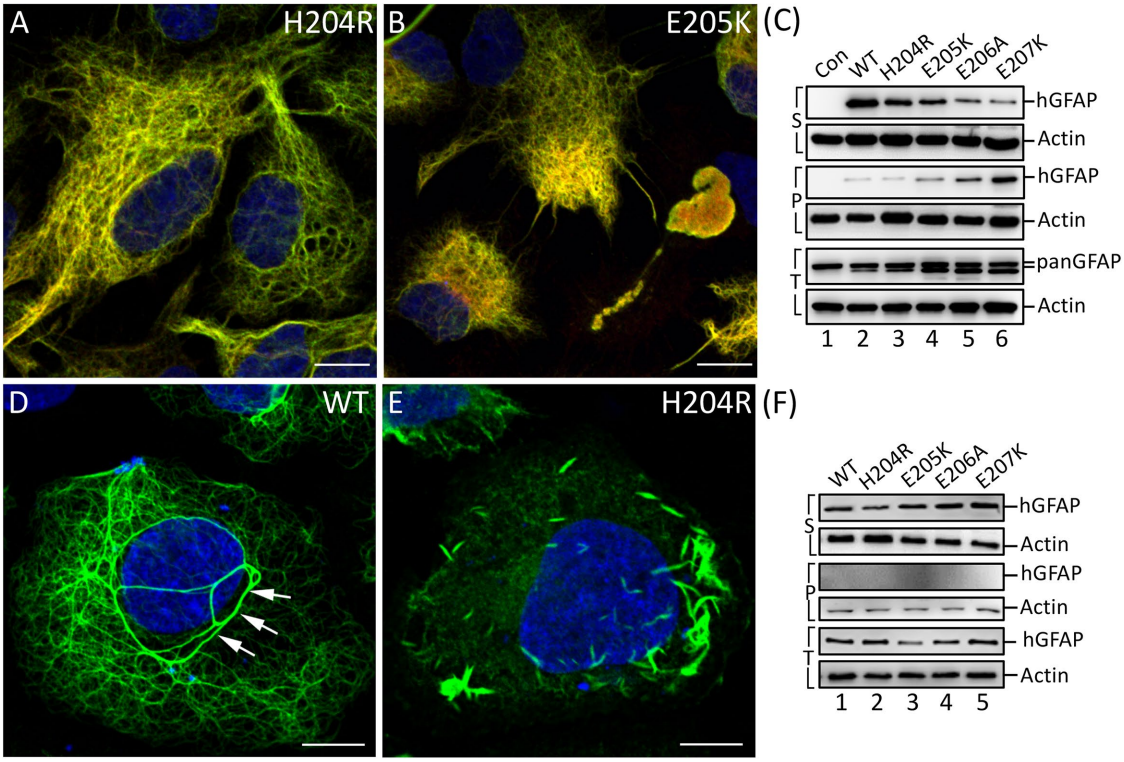

FIGURE 6: Filament organization and solubility properties of GFAP internal rod mutants. (A, B) Primary astrocytes were transduced with the indicated GFAP mutants for 72 h. Cells were fixed and immunostained with anti-hGFAP (green channel) and anti-panGFAP (red channel) antibodies. Nuclei were visualized by staining with DAPI (blue channel), and merged images are shown. Bar, 10 μm. (C) Cells transduced with the empty vector (lane 1) or the indicated GFAP constructs (lanes 2–6) were extracted, and the resulting supernatant (S) and pellet (P) fractions were analyzed by immunoblotting with anti-hGFAP antibody. Total GFAP (T) in the whole cell lysates was analyzed by the anti-panGFAP antibody. Sample loading: 3.12 μg of protein per lane for the supernatant (S); 2.56 μg of protein per lane for the pellet (P); 5.14 μg of protein per lane for the total (T). (D, E) IF-free SW13 (vim-) cells were transiently transfected with either WT (D) or H204R mutant (E) GFAP. At 48 h after transfection, cells were fixed and immunostained with the anti-hGFAP antibody (green channel) and counterstained with DAPI (blue channel). Merged images are shown. Bar, 10 μm. (F) Cells transfected with either WT (lane 1) or mutant (lanes 2–5) GFAPs were extracted, and the total (T), supernatant (S), and pellet (P) fractions were analyzed by immuboblotting using the anti-hGFAP antibody. Actin was used as a loading control for these samples.

and E207K (Figure 6C, lane 6) GFAP. This is in contrast to cells transduced with WT (Figure 6C, lane 2) and H204R (Figure 6C, lane 3) GFAP, which were almost completely extracted into the soluble fraction. Analysis of the total cell lysates revealed that levels of transduced GFAP increased between 0.5 and 1.2 fold (Figure 6C, lanes 2–6) over the endogenous baseline levels (Figure 6C, lane 1).

To ascertain whether H204R mutation might have subtle effects on GFAP network formation that we could not detect in primary astrocytes, we repeated our experiments in SW13 (vim-) cells. These cells, which express no endogenous cytoplasmic IFs (Hedberg and Chen, 1986), have proved to be more sensitive for revealing alterations in network formation of mutant GFAP than in cells that express preexisting filament networks (Perng *et al.*, 2006). When transfected into this cell line, WT GFAP mainly formed filament networks (Figure 6D), although filament bundles were often observed (Figure 6D, arrows). In contrast, the H204R mutant formed short needle-like structures (Figure 6E) with no obvious filamentous networks typical of WT GFAP. A similar staining pattern was also seen for cells transfected with E205K, E206A, and E207K (Supplemental Figure S6, C–E) mutant GFAP. When cells were extracted using the same extraction protocol for primary astrocytes, both WT and mutant GFAP were found exclusively in the soluble fraction (Figure 6F).

GFAP accumulates in the RFs of the AxD patient brain

Given that AxD mutations at highly conserved rod ends perturbed filament assembly in a way that promotes GFAP aggregation, we tested whether these mutants could form GFAP aggregates in the form of RFs in brains from human AxD patients. Available brain tissues from four AxD patients who carried different GFAP mutations were analyzed, along with four age-matched non-AxD controls (Table 1). Protein samples were prepared by a fractionation protocol (Lin *et al.*, 2021) that extracted normally polymerized GFAP into the urea-soluble fraction (Supplemental Figure S7) while retaining urea-insoluble GFAP in the RF fraction (Figure 7). Immunoblotting analysis of the RF-enriched fractions revealed that GFAP levels were highly elevated in all AxD brain tissues (Figure 7A, lanes 5–8) compared with non-AxD controls (Figure 7A, lanes 1–4). A high-molecular-weight GFAP smear as well as a series of 37–45 kDa degradation products were also detected in these samples (Figure 7A, lanes 5–8, asterisks). Notably, the elevated GFAP levels in the RF fractions correlated with the detection of increased levels of αB-crystallin and high-molecular-weight ubiquitinated proteins (Figure 7A, lanes 5–8), previously known components of RFs. Analysis of the Coomassie blue–stained gel revealed that RF-enriched fraction contained 45.2% of GFAP in the L76V sample, 38.4% in the N77S sample,

Case	Mutation	Cause of death	Age at death, yr	Sex
Control 1	—	Drowning	2	M
Control 2	—	Asphyxia by hanging	13	M
Control 3	—	Head and neck injury	28	F
Control 4	—	Head injuries	29	M
AxD 1	L76V	Infantile onset/type I	10.5	F
AxD 2	N77S	Infantile onset/type I	2	F
AxD 3	R79C	Juvenile onset/type II	14	M
AxD 4	L359V	Juvenile onset/type II	20	M

TABLE 1: Clinical and genetic details of patient samples used in this study.

34.3% in the R79C sample, and 31.5% in the L359V sample (Figure 7B, lanes 5–8), whereas less than 1% of GFAP was detected in non-AxD controls (Figure 7B, lanes 1–4). Thus, most of the GFAP analyzed for the AxD samples was presumably in the RF fraction, but few if any of these aggregates were present in the non-AxD controls.

Because AxD mutations could cause GFAP aggregation not through the predicted amino acid change but by altering splicing to increase the level of GFAP isoforms (Helman *et al.*, 2020), we examined whether elevated expression of GFAP isoforms is responsible for RF formation. The unique C-terminal tail of GFAP-δ had allowed a polyclonal antibody to be raised against the last 12 amino acids of this isoform. The affinity and specificity of this antibody were confirmed by immunoblotting of purified recombinant GFAP-δ (Supplemental Figure S8B, lanes 5–8), complementing a monoclonal antibody specific to GFAP-α (Supplemental Figure S8A, lanes 1–4). Immunoblotting analysis of RF-enriched fractions revealed the presence of GFAP-δ in the AxD brain tissues (Figure 7A, lanes 5–8). A higher GFAP band recognized by both anti–GFAP-δ and anti–GFAP-α antibodies was also detected (Figure 7A, lanes 5–8), consistent with the expression of GFAP-λ (Helman *et al.*, 2020). Using known amounts of purified recombinant human GFAP isoforms as standards (Supplemental Figure S8, C and D), the average levels of GFAP-δ and GFAP-λ in AxD brain samples were estimated to be 5.4 ± 1.27 and 1.7 ± 1.27%, respectively, of the GFAP-α. These results suggest GFAP accumulation in the RFs is likely due to GFAP mutation per se rather than disproportionally increased expression of minor GFAP isoforms.

DISCUSSION

This is the first comprehensive investigation of the effects of AxD-associated mutations located in the rod domain of GFAP. Our in vitro study showed that the assembly behaviors of individual GFAP mutants are complex, as some of them did not assemble beyond the ULF state whereas others assembled into abnormal filaments that are prone to aggregation. Accordingly, these GFAP variants are classified into four distinct assembly groups (Table 2).

The first group of mutants (N77K, D78Y, R79C, R79H, and L357P GFAP) assembled into ULF-like structures but failed to longitudinally anneal, so that their assembly stopped at this stage. The second group (Y366H GFAP) formed ULF-like assemblies that had a strong tendency to aggregate. The third group (L76V, H204R, E205K, E206A, E207K, L359P, and L369P GFAP) did form ULFs, but after elongation at a certain length not only longitudinal annealing but also radial compaction were compromised. The resulting filaments were short and retained their ULF diameter. The fourth group of mutants (L352P and L353P GFAP) formed filamentous materials that self-associated into large aggregates, from which single filaments occasionally protruded. In addition, the width control of both mutants appeared to be impaired compared with WT GFAP as filaments often exhibited a larger diameter. A schematic diagram (Figure 8) summarizes the main steps of GFAP assembly based on the pathway originally described for vimentin (Herrmann and Aebi, 2004) and desmin (Bar *et al.*, 2005). GFAP mutants deviating from the normal assembly pathway at distinct steps are indicated, highlighting the inability of these mutants to perform the appropriate subunit reorganizations needed to reach the next assembly stage. Some GFAP mutants

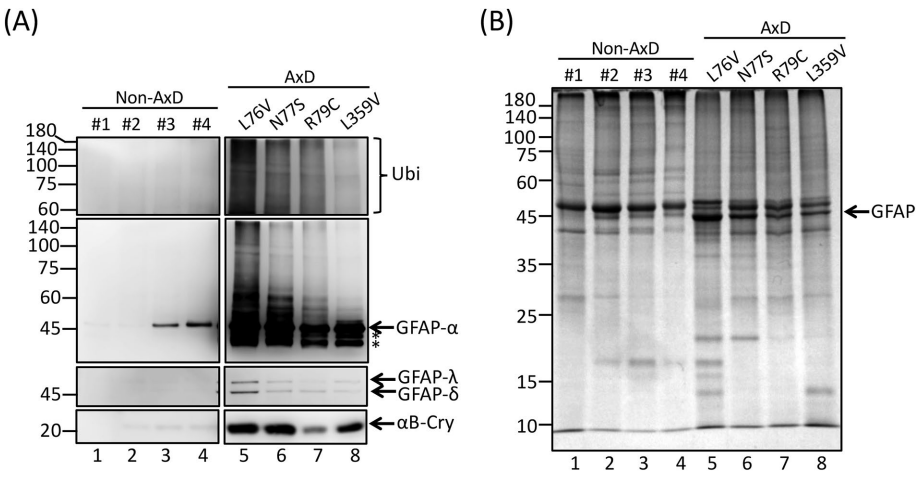

FIGURE 7: Accumulation of GFAP mutants in the RFs of human AxD brain samples. (A) Brain tissues from four non-AxD controls (lanes 1–4) and four AxD patients (lanes 5–8) were sequentially extracted with buffers of increasing extraction strength. The urea-insoluble RF fractions were analyzed by immunoblotting using antibodies specific to GFAP-α, GFAP-δ, ubiquitin, and αB-crystallin. The presence of GFAP-λ was confirmed by immunopositive detection of samples with both anti–GFAP-α and anti–GFAP-δ antibodies. Asterisk (*) indicates GFAP degradation products. (B) Proteins in the RF fraction were analyzed by SDS–PAGE, followed by Coomassie blue staining. Approximate molecular weight markers (in kDa) are shown on the left, and the position of GFAP is indicated. Note that the protein loading amounts for immunoblotting (A) and Coomassie blue staining (B) were 1 and 10 μg, respectively.

Location	Mutation	Repeat position[a]	In vitro assembly	Lentiviral transduction	RIPA extractability[b]
—	WT (no mutation)	—	Typical 10-nm filaments	Normal IF networks	High[c]
Group I: Formation of ULF-like structures that failed to elongate					
Coil 1A	N77K	e	ULFs and short filaments[d]	Aggregates with granular structures	Low[e]
Coil 1A	D78Y	f	ULFs and short filaments	Aggregates with granular structures	High
Coil 1A	R79C	g	ULF-like structures	Aggregates with oval shapes	Low
Coil 1A	R79H	g	ULF-like structures	Aggregates with ring-like structures	Low
Coil 2	L357P	b	ULFs and short filaments	Large cytoplasmic aggregates	Low
Group II: Association of ULF-like structures into aggregates					
Coil 2	Y366H	d	Nonfilamentous aggregates	Large cytoplasmic aggregates	Low
Group III: Impaired longitudinal annealing and disturbed radial compaction					
Coil 1A	L76V	d	Short irregular filaments	Aggregates with dot-like structure	Low
Coil 1B	H204R	h	Short filaments	Normal IF networks	High
Coil 1B	E205K	i	Short unraveled filaments	Aggregates and IF networks	Medium[f]
Coil 1B	E206A	j	Short unraveled filaments	Aggregates and IF networks	Medium
Coil 1B	E207K	k	Tapered rod-like structures	Aggregates and IF networks	Low
Coil 2	L359P	d	Short irregular filaments	Large cytoplasmic aggregates	Low
Coil 2	L369P	g	Filaments with uneven width	Large cytoplasmic aggregates	Low
Group IV: Enhanced filament self-association leading to uncontrolled aggregation					
Coil 2	L352P	d	Filamentous aggregates	Large cytoplasmic aggregates	Low
Coil 2	L353P	e	Filamentous aggregates	Large cytoplasmic aggregates	Low

[a]Repeat position: GFAP rod domain is α-helical in nature with periodic patterns, namely a seven-residue heptad repeat (designated a,b,c,d,e,f,g) and an 11-residue hendecad repeat (designated a,b,c,d,e,f,g,h,i,j,k), which is equivalent to an extension of four residues from the end of a heptad.
[b]RIPA: radioimmunoprecipitation assay.
[c]High: >75% GFAP in the supernatant.
[e]Low: <25% GFAP in the supernatant.
[c]High: >75% GFAP in the supernatant.
[f]Medium: 25%–75% GFAP in the supernatant.

TABLE 2: Effect of GFAP mutations on filament assembly in vitro and in astrocytes.

act in a dominant manner that drives the WT protein into non-IF structures. These in vitro studies were corroborated by transducing GFAP into primary astrocytes, which revealed that assembly-compromised GFAP mutants mainly formed cytoplasmic aggregates that disrupted the endogenous IF networks and were more resistant to solvent extraction.

How AxD mutations in coil 1A compromise GFAP assembly

IF proteins feature a central α-helical domain, within which amino acids are organized in consecutive groups of heptads, such that every first and fourth amino acid is usually hydrophobic. This organization results in a hydrophobic stripe that allows two chains to form a coiled-coil dimer. Based on the sequence homology of many IF proteins, two so-called IF consensus motifs became evident: one close to the amino-terminal end of the rod within coil 1A, and another marking the end of coil 2. IFs are believed to elongate through head-to-tail interactions involving an overlap of the coil 1A and coil 2 end regions (Fuchs, 1996; Parry and Steinert, 1999). This interaction likely explains the especially strong sequence conservation of these segments and the clustering of disease-causing mutations in these regions in both AxD and other genetic disorders of IFs (Omary *et al.*, 2004).

In GFAP, the conserved N-terminal region spans amino acids 72–86 and contains the highly conserved LNDR sequence that is present in almost all IF proteins. Mutations within this region, spanning amino acids 76–79 of human GFAP, interfered drastically with the IF assembly. Judging from the crystal structure of human vimentin, an IF protein closely related to GFAP, change in the highly conserved leucine at L76, which occurs in the d position of coil 1A, should have little or no influence on the coiled-coil geometry. However, a subtle change in the hydrophobic seam as a result of L76V mutation may have a destabilizing effect on the coiled-coil segment (Meier *et al.*, 2009). The dimer is also stabilized by intrachain and interchain ionic interactions formed between polar residues. The N77 residue, located in an e position of a heptad, aligns along one side of the helix, allowing its side chain to interact within the filament. Substitution of the N77 to the positively charged lysine may interfere with ionic interactions between individual coiled-coil chains necessary for the molecular rearrangements taking place both during the lateral association and the elongation phase of assembly. In addition, the N77K mutation could change the surface charge pattern of the filaments, which could translate into different binding features that potentially alter interactions of GFAP with its binding partners, such as signaling molecules and

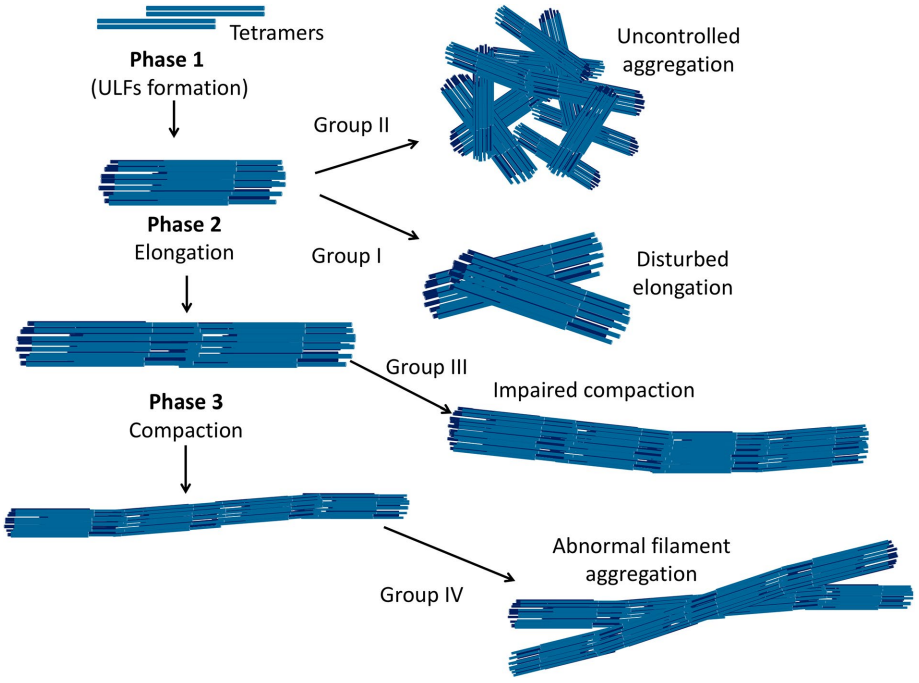

FIGURE 8: Schematic representation of the assembly process of GFAP and specific steps that mutations interfered with GFAP assembly. The in vitro assembly process of GFAP filaments follows three major steps, that is, ULF formation, longitudinal annealing, and radial compaction. The 14 mutant GFAP variants assembled into various IF-like and non-IF structures (Table 2), and hence they are grouped into four distinct assembly groups. The points of deviation from which the first divergences from the normal assembly pathway become apparent are indicated. The first group of mutants (I) assembled into ULF-like structures that failed to anneal longitudinally; the second group of mutants (II) formed ULFs that are prone to aggregation; the third group of mutants (III) affected both elongation and compaction of filaments; the fourth group of mutants (IV) formed abnormal filaments that are prone to aggregation.

chaperones (Supplemental Table S1), as has been suggested for keratins (Lee *et al.*, 2019) and other IFs (Ivaska *et al.*, 2007).

Change at the R79 can be severe, probably because it resides at the g position of the first heptad that is part of the coil 1A initiator region. Substitution of the R79 with either cysteine or histidine may potentially disrupt the intrahelical salt bridge between R79 and E75 (Herrmann and Aebi, 2004), thereby compromising the stability of the tetrameric complexes in a way that prevents proper longitudinal annealing of the ULFs into extended filaments. Homologous mutation that was introduced into keratin 18 (Hesse *et al.*, 2007), vimentin (Hess *et al.*, 2005; Schietke *et al.*, 2006), and desmin (Herrmann and Aebi, 2004) demonstrated that this arginine residue is of general importance for IF assembly because it completely impeded filament formation in vitro. Interestingly, transgenic mice that expressed the mutated form of vimentin caused a disease phenotype specifically in the eye lens leading to a posterior cataract, highlighting the pathogenic potential of this mutation in vivo (Bornheim *et al.*, 2008).

In the context of the cell, all LNDR mutants formed GFAP aggregates, which were more resistant to biochemical extraction. However, although the D78Y mutant also formed aggregates when expressed in primary astrocytes, it was extracted into the soluble fraction. One potential mechanism linking the solubility property and IFs is an alteration of phosphorylation (Snider and Omary, 2014). GFAP is phosphorylated at multiple sites by several kinases (Supplemental Table S2), and this modification may impact the assembly properties and biological functions of this IF protein (Sihag *et al.*, 2007). Changing the aspartic acid to a tyrosine not only introduces a steric interference but may also alter the status of GFAP phosphorylation and thereby disturb filament organization. Given that increased phosphorylation of GFAP is causally associated with RF formation particularly in the early-onset forms of AxD (Battaglia *et al.*, 2019), excessive phosphorylation of tyrosine on GFAP (Rikova *et al.*, 2007) could result in its chronic presence in an incompletely polymerized state, leading to short filaments that are prone to aggregation.

How the C-terminal rod mutations cause GFAP assembly defects

The C-terminal end of GFAP extends from amino acid 363 to amino acid 376, containing the highly conserved TYRKLLEGEE motif that overlaps with the trigger sequence in this region. This dual function may explain the clustering of severe cases of AxD caused by GFAP mutations in or near this motif. Notably, GFAP mutations associated with severe clinical phenotypes and a rapid disease progression usually involve the replacement of leucine, which is often situated in an a or d position of a heptad, by proline near this region. For instance, Bassuk *et al.* (2003) reported an infantile case of AxD carrying an L352P mutation, which was the most severe case of any described with onset at birth and death at 38 d of age. The especially devastating consequences of these leucine-to-proline mutations (L352P, L353P, L357P, L359P, L369P) could be explained by the fact that proline acts as a helix breaker that locally disrupts or at least kinks the α-helical structure at the rod end (Barlow and Thornton, 1988). In addition, its cyclic side chain blocks the central nitrogen atom, thus preventing it from forming a stabilizing hydrogen bond (Krieger *et al.*, 2005; Morgan and Rubenstein, 2013). Such structural alterations within the coiled-coil can destabilize its local conformation and exert deleterious effects on filament assembly (Gromiha and Parry, 2004; Smith *et al.*, 2004). The disruptive effect of the proline on the normal coiled-coil geometry may also explain its evolutionarily conserved exclusion from α-helices of the rod domain.

Our data show that changing the precise sequence of this region has a dramatic effect on GFAP assembly. For instance, both L352P and L353P mutants formed thick filament bundles that had a strong tendency to aggregate both in vitro and in astrocytes. While no disease-associated mutation homologous to the L352P has been identified in any of the known IF proteins, the L353P mutation has a high level of conservation among other IF proteins. A change in the equivalent leucine to proline (L387P) in vimentin caused a multisystem disorder associated with frontonasal dysostosis and premature aging (Cogne *et al.*, 2020). The L387P mutation dramatically disturbed vimentin filament assembly and organization, resulting in the accumulation of abnormal aggregates in transfected cells. In a zebrafish model, this mutant impaired craniofacial development, peripheral axon branching, and body fat distribution, similar to those phenotypes observed in the human patient. Corresponding mutations in desmin (L392P) and keratin 17 (L371P) are associated with myofibrillar myopathy (Olive *et al.*, 2007) and

steatocystoma multiplex (Gass *et al.*, 2009), respectively. Although the functional effects of these mutants have yet to be tested, our data suggest that this residue is of general importance in the assembly of IFs. This is supported by the structural modeling of crystalized vimentin coil 2 (Nicolet *et al.*, 2010), where changing the L387 residue located in an e position of a heptad to an α-helical perturbing residue could interfere with its side chain to interact within filaments and affect higher-order organization in a way that promotes filament self-associations.

The YRKLLEGEE motif at the C-terminal end of the rod domain is highly conserved, suggesting that it plays an essential role common to all IF proteins. Our data showed that GFAP mutations within this motif dramatically alter filament assembly both in vitro and in transduced astrocytes and do so in a dominant manner. Substitution of Y366 residing in a d position of a heptad with histidine interfered with GFAP assembly to the extent that both the longitudinal annealing of the ULF-like precursors into long filaments and the lateral integrity of the resulting filaments were disturbed. A homologous mutation in vimentin causes an assembly arrest at the ULF stage, demonstrating an important role of this tyrosine residue during the elongation phase of IF assembly in vitro (Premchandar *et al.*, 2016). Structural studies on vimentin coil 2 revealed that the two α-helices gradually fold away from the coiled-coil axis at Glu405 because of the repulsion within the following acidic cluster (Herrmann *et al.*, 2000; Strelkov *et al.*, 2002). The splaying may facilitate an interdigitating head-to-tail arrangement of coils 1A and the C-terminus of coil 2 into an overlapping cross-coil (Smith *et al.*, 2002), which stabilizes tetramers in the transition from ULFs to filaments (Chernyatina *et al.*, 2015). These findings thus indicate that the inability of the Y366H GFAP mutant to form filaments may originate from local changes in the α-helical stability and flexibility at the end of coil 2, leading to its inability to properly engage in the interactions with coil 1A.

In addition, our coassembly studies using a peptide containing the coil 2 consensus sequence showed that this peptide was able to compete with the endogenous sites on GFAP to interfere with filament formation in vitro and to cause disassembly of preformed filaments. These results suggest that the consensus motif at the end of coil 2 is actively involved in molecular contacts that stabilize different oligomeric forms such as tetramers, ULFs, and mature filaments. Recent study on the crystal structures of keratins identified such contacts at the end of coil 2 that may play an important role in higher-order IF assembly (Lee *et al.*, 2020; Lomakin *et al.*, 2020). Mutations in this region impaired the ability of keratins to assemble into normal 10-nm filaments, supporting a crucial role of these molecular contacts in nucleation and stabilization of coiled-coil dimers through a network of ionic and hydrophobic interactions.

Effects of the GFAP mutations more internal to the rod domain

Changing the precise sequence of coil 1B also affects GFAP assembly. Our in vitro assembly studies show that mutations in this region partially inhibit filament assembly but do not block it completely. One likely explanation for this assembly defect is that these mutations may destabilize interdimeric interactions in a way that alters the normal process of filament assembly, a suggestion now supported by the crystal structure analysis of GFAP (Kim *et al.*, 2018).

Coil 1B of GFAP contains a hendecad, which is equivalent to a heptad extended by four residues (H204–E207) denoted as h-i-j-k (Gruber and Lupas, 2003). Although this region is not assigned as a heptad repeat, it adopted an extended α-helix and contributed to the formation of the continuous coiled-coil. Mutations in coil 1B of GFAP may alter the IF structure in a variety of ways. For instance, the H204 at the h position of a hendecad lies within the hydrophobic interface and plays a key role in maintaining the coiled-coil geometry through stacking interactions between the two imidazole rings. Changing the H204 to arginine may disrupt the interdimeric interactions, thereby destabilizing the tetrameric complexes. Both the E205K and the E207K mutations involve a reversal of charge, and this alteration may change the local electrostatic potential at the surface that affects the lateral association of GFAP tetramers. In particular, the E207K mutation would eliminate the stabilizing ionic interaction with H204 in the coiled-coil interface. This change could induce a local helix kinking to avoid charge repulsion or steric clashes. Changing the E206 residue to a small alanine may disrupt its interaction with the V115 in the adjacent dimer, thereby causing distortion of the helical structure that could perturb the dimer–dimer interface. Collectively, modeling AxD-associated mutations based on the GFAP 1B crystal structure suggests that mutations in this region are likely to distort the fundamental helical structure and destabilize inter- and intramolecular interactions in the GFAP dimer and tetramer. One implication from this model is that GFAP mutations within coil 1B could cause AxD by reducing the rate or efficiency of GFAP assembly, thereby causing aberrant IF formation in vitro and in cells.

In the context of the astrocytes, the effects of GFAP 1B mutations on IF network formation were less severe than those residing at both ends of the rod. While the E205K, E206A, and E207K mutants formed cytoplasmic aggregates in less than 30% of transduced astrocytes, the H204R GFAP assembled into normal IF networks that were indistinguishable from the WT. However, transient transfection of the H204R mutant into IF-free SW13 cells resulted in formation of unusual needle-like short filaments rather than the extended IF networks formed by the WT GFAP. These short and discontinuous filament fragments were also observed in cells transfected with E205K, E206A, and E207K mutant GFAP. These structures are somewhat reminiscent of what have previously been reported for a splice site mutation that results in an internal truncation of coil 1B (Flint *et al.*, 2012) and an E210K mutation residing within this region (Li *et al.*, 2005), suggesting that perturbation of the coil 1B structure leads to their formation.

How can we apply our knowledge of GFAP structure and assembly to understand disease pathology at the tissue level?

In human AxD brain tissues, analysis of RF fractions revealed that GFAP levels were highly elevated compared with those of non-AxD controls. These results are consistent with previous studies (Walker *et al.*, 2014; Battaglia *et al.*, 2019; Helman *et al.*, 2020), but mechanisms leading to GFAP elevation remain unknown. Given that GFAP is itself a stress protein (Toivola *et al.*, 2010) and is up-regulated in response to reactive astrocytes, it is no surprise that GFAP levels increase. Increased levels of GFAP mRNA had previously been reported in two AxD patients (Hagemann *et al.*, 2005), suggesting that increased GFAP synthesis is at least one mechanism contributing to the overall change in total levels. A number of feed-forward processes have been proposed whereby GFAP mutation and its subsequent accumulation cause pathological changes such as induction of autophagic (Tang *et al.*, 2008) and immune-related (Olabarria *et al.*, 2015) responses and inhibition of proteasome activity (Tang *et al.*, 2006), leading to a further increase in GFAP production.

GFAP levels are indeed elevated in AxD, but the actual ratio of mutant to WT protein remains unknown. In one study using an

antibody specific for a disease-causing R416W GFAP, Perng *et al.* (2006) showed that the mutant protein was incorporated into both the normal-appearing filament bundles and the RFs in an AxD patient carrying this mutation. Although this study did not determine the ratio between WT and mutant in this patient, coassembly titrations showed that having just 25% mutant protein was sufficient to abolish the normal filament assembly process in vitro. Using mass spectrometry to analyze GFAP in autopsy tissues from three AxD patients, Heaven *et al.* (2019) showed that the levels of mutant GFAP were lower than those of the WT, suggesting that even a small amount of mutant protein is sufficient to produce disease. In another study, analysis of the brain mRNA from an AxD patient with an unusual splice site mutation revealed a WT-to-mutant transcripts ratio in the range of 12 to 1 (Flint *et al.*, 2012). Using a cell culture model to study the dominant effect of this mutation, they found that this mutant at a level 2.5% of the total could disrupt IF network formation. Because GFAP mutation could act at the nucleotide level to alter mRNA splicing (Helman *et al.*, 2020) or stability (Flint *et al.*, 2012), mutation-induced unequal allelic expression of WT versus mutant GFAP may represent a new pathogenic factor for AxD. The imbalanced ratio of WT to mutant GFAP may provide an explanation for the otherwise puzzling observation that total GFAP levels are actually decreased in the spinal cord of AxD mice compared with the WT (Chen *et al.*, 2013; Jany *et al.*, 2013), despite the clear presence of RFs in this region.

GFAP normally exists in dynamic equilibrium between the soluble and insoluble pools, but how AxD mutations decreased the solubility of GFAP leading to a shift in equilibrium toward the insoluble pool remains unknown. Using a urea extraction protocol to distinguish between GFAP in normal filaments and that in RFs (Heaven *et al.*, 2016), we found that GFAP in the AxD brains was fractionated primarily into the urea-insoluble RF fraction. One possible explanation for the increased resistance of GFAP to urea extraction is that the presence of mutant protein could change filament properties in a manner that promotes GFAP aggregation through increased filament–filament interactions. Another likely explanation is that an increase of GFAP in the RF fraction may simply reflect an elevated expression of minor GFAP isoforms, as occurred in a recently reported AxD patient (Helman *et al.*, 2020). However, our data do not support this possibility. Both GFAP-δ and GFAP-λ were detected in the RF fraction of AxD tissues, but they were up-regulated coordinately with GFAP-α. Although both were easily detected as total GFAP levels were highly elevated, they were expressed at levels lower than 10% of the total, similar to those observed in the normal human brain (Roelofs *et al.*, 2005) and spinal cord (Perng *et al.*, 2008). Thus, GFAP elevation and accumulation as RF is caused by the mutant GFAP per se, rather than a shift in ratio in favor of minor isoform expression.

Alternatively, GFAP could become preferentially enriched in the RF fraction if its urea solubility was reduced in the AxD brain tissues by means other than increased self-association, for example, by a change in interaction with binding partners (Supplemental Table S1) or posttranslational modifications (Supplemental Table S2). Our data show that the levels of GFAP in RF fractions of AxD patients correlated with the detection of increased accumulation of insoluble αB-crystallin (αB-cry) and ubiquitin (Figure 7A), previous known components of RFs. The small heat shock protein αB-cry is an IF-binding protein with an important role in regulating GFAP assembly (Perng *et al.*, 1999), and its elevation is a consistent feature of AxD. The accumulated αB-cry in the RF fraction suggests its up-regulation in response to GFAP aggregation, which is consistent with previous reports (Goldman and Corbin, 1991; Heaven *et al.*, 2016; Lin *et al.*, 2021). In studies with AxD mouse models, RFs appear to originate as local granules composed of GFAP and αB-cry deposited on preexisting IFs (Sosunov *et al.*, 2017). The presence of αB-cry in early RFs likely reflects its function as a sensor for detecting misfolded assembly intermediates and binding to filaments with altered architecture (Sharma *et al.*, 2017). The sequestration of αB-cry into RFs may compromise its normal function, such as alleviating a mutant GFAP-induced proteasome inhibition (Tang *et al.*, 2010), and thereby aggravate the effects of GFAP accumulation in inhibiting proteasome activities (Tang *et al.*, 2006). Indeed, we found that GFAP accumulation in the RF fraction increased levels of high-molecular-weight ubiquitinated proteins, suggesting impaired proteasome activity in astrocytes of AxD.

Conclusion

In summary, we provide the clinically relevant evidence that links GFAP assembly defects to disease pathology at the tissue level. Our studies support the conclusion that amino acids throughout the rod domain of GFAP are not equal with respect to their roles in filament assembly and network formation. However, we are unable to explain why some amino acids exchange results in a drastic assembly defect, whereas others allow filament formation that are prone to aggregation. A more rational understanding of the underlying molecular mechanisms requires the structural detail of GFAP and an atomic model of the glial filament. This knowledge will be of importance in the structure-based understanding of GFAP assembly, setting up the foundation for further investigation of the consequences of GFAP mutation–induced assembly defects on the astrocyte and CNS functions.

MATERIALS AND METHODS

Plasmid construction and site-directed mutagenesis

Nucleotide changes encoding specific amino acids were engineered by site-directed mutagenesis using the InFusion HD Plus Cloning System (Takara Bio, Mountain View, CA). GFAP mutations were introduced directly into the cDNA of human WT GFAP in the pLEX MCS vector (Lin *et al.*, 2016) for lentiviral transduction, in the pcDNA 3.1 (–) vector for transient transfection (Perng *et al.*, 2006), and in the pET23b vector for bacterial expression (Chen *et al.*, 2011). All newly constructed vectors containing the mutation were confirmed by DNA sequencing before use.

Expression and purification of recombinant GFAPs

For bacteria expression of GFAP, pET23b vector containing either WT or mutant GFAPs was transformed into the *Escherichia coli* BL21 pLysS strain (Agilent Technologies, Santa Clara, CA). Induction of recombinant protein overexpression was achieved by the addition of 0.5 mM Isopropyl 1-thio-β-D-galactopyranoside (IPTG) when the optical density (OD_{595}) reached 0.2. After incubation for an additional 4 h, bacteria were harvested by centrifugation at 6000 × *g* for 30 min at 4°C. Overexpressed GFAP formed inclusion bodies, which were prepared as described previously (Perng *et al.*, 2006). The final pellets, consisting predominantly of GFAP, were extracted in urea buffer (6 M urea, 20 mM Tris-HCl [pH 8], 5 mM EDTA, and 1 mM phenylmethylsulfonyl fluoride [PMSF]) at 4°C overnight. After centrifugation at 80,000 × *g* for 20 min at 4°C, the urea-soluble fractions were treated with 0.05% (vol/vol) polyethyleneimine (PEI; Sigma-Aldrich, St. Louis, MO) to precipitate contaminating bacterial DNA. After centrifugation under the same conditions, GFAP in the supernatant was further purified by anion-exchange chromatography using an AKTAprime plus system (GE Healthcare, Chicago, IL). GFAP was eluted from a DEAE Sepharose (GE Healthcare) column with a linear gradient of 0–1 M

NaCl in the urea buffer over 1 h at a flow rate of 1 ml/min. Column fractions were analyzed by SDS–PAGE followed by Coomassie brilliant blue staining, and those containing purified GFAP were pooled and stored at −80°C. The protein concentration was determined by bicinchoninic acid assay (BCA) assay (Thermo Fisher Scientific, Waltham, MA) using bovine serum albumin (BSA) as a standard.

Production of GFAP coil 2 fragment

Using the full-length human GFAP cDNA as a template, the coil 2 fragment, corresponding to amino acids 257–370 of human GFAP, was amplified by PCR using oligonucleotides 5′-TTATATTTTCAAGGGTACCGCTCCAAGTTTGCAGACCT-3′ and 5′-ATCTTAGAATT CTCATAGCAGCTTCCTGTAGGTGGC-3′ as forward and reverse primers, respectively. The amplified PCR product was cloned into the prokaryotic expression vector pPEP-Tev (Addgene #38037) using the InFusion System. The expression construct encodes a fusion protein containing an N-terminal 6xHis-tag, a laminin spacer (5 kDa), and a tobacco etch virus (TEV) protease cleavage site followed by the coil 2 fragment. The entire sequence of the construct was verified by DNA sequencing before use.

Overexpression of the coil 2 fragment was induced using the same procedure as described above, except that bacteria were incubated at 16°C overnight after IPTG induction. Bacteria were collected and lysed by homogenization in urea buffer (8 M urea, 40 mM Tris-HCl, pH 8, 50 mM NaCl, 5 mM β-mercaptoethanol, and 2 mM PMSF) containing 10 mM imidazole. Total lysates were centrifuged at 16,400 × *g* for 20 min at 4°C, and the resulting supernatant was treated with 0.05% (vol/vol) polyethyleneimine (PEI) to precipitate contaminating bacterial DNA. After PEI precipitation, the urea-soluble fraction was loaded onto a Ni Sepharose column (GE Healthcare), followed by elution with 250 mM imidazole in urea buffer. Purified protein was pooled, dialyzed into the cleavage buffer (50 mM Tris-HCl, pH 8, 40 mM NaCl), and digested at 30°C overnight with the Tev protease, which was produced recombinantly in bacteria using an expression vector (pRK793 from Addgene; #8827) and purified by a chelating column charged with Ni. A second Ni Sepharose column was then used to remove His-tag–containing fragments. The purified GFAP fragment was pooled and concentrated by centrifugal concentrators (Millipore; 3.5 kDa cutoff), and the protein concentration was determined by BCA assay using bovine serum albumin (BSA) as a standard.

In vitro assembly and sedimentation assay

In vitro assembly of GFAP was carried out as described previously (Chen *et al.*, 2011). Briefly, purified GFAP was diluted to 0.3 mg/ml in 6 M urea in a low-salt buffer (10 mM Tris-HCl [pH 8.0], 5 mM EDTA, and 1 mM dithiothreitol [DTT]) and dialyzed stepwise against 3 M urea in the same buffer for 4–6 h at room temperature and then against the same buffer without urea overnight at 4°C. Filament assembly was completed by dialyzing against assembly buffer (10 mM Tris-HCl, 50 mM NaCl, 1 mM DTT, pH 7 ± 0.05) for 12–16 h at 28–30°C. Assembly efficiency was assessed by high-speed centrifugation at 80,000 × *g* for 20 min at 22°C (Nicholl and Quinlan, 1994). Filament-forming efficiency was defined as the percentage of pellet protein contained in the total. To investigate the effect of mutations on GFAP aggregation, assembly mixtures were subjected to a low-speed centrifugation at 800 × *g* for 5 min at room temperature using a benchtop centrifuge (Eppendorf; 5415R). The supernatant and pellet fractions were analyzed by SDS–PAGE, followed by Coomassie brilliant blue staining. Signals for individual bands in the stained gel were quantified using ImageQuant software (Ver. 7.0; GE Healthcare, Chicago, IL).

Cosedimentation assay

GFAP coil 2 fragment was mixed with WT GFAP in 10 mM Tris-HCl, pH 8.0, 5 mM EDTA, 1 mM DTT and then dialyzed into 10 mM Tris-HCl, pH 7.0, 5 mM EDTA, 1 mM DTT. Assembly of the GFAP in the absence or presence of the coil 2 fragment was completed by dialyzing against 20 mM imidazole-HCl, pH 6.8, 100 mM NaCl, 1 mM DTT at 37°C for 16 h. In some experiments, GFAP was assembled first, followed by incubation with the coil 2 fragment at 37°C. After incubation for 3 h, assembly mixtures were subjected to a high-speed centrifugation at 80,000 × *g* for 20 min, and the supernatant and pellet fractions were compared by SDS–PAGE and Coomassie blue staining.

Transmission electron microscopy

For negative-staining transmission electron microscopy, samples were spread on 300 meshed formvar/carbon film–coated copper grids (Ted Pella, Redding, CA) for 5 min, washed once with distilled water for 1 min, stained with 1% (wt/vol) uranyl acetate for 3 min, and visualized under an Hitachi H-7700 electron microscope (Hitach High-Tech, Japan) operating at 100 kV. Images were acquired using a charge-coupled device camera before being processed further for figures using Adobe Photoshop CC (Adobe System, San Jose, CA).

To quantitate filament width and length, random series of at least five electron micrographs were selected from each in vitro assembly experiment. Widths were measured from 12–15 randomly selected filaments, and quantitative analyses were made using ImageJ software. Because of the aberrant associations of many mutant GFAP filaments, the true length of GFAP filaments was difficult to assess. Therefore, lengths were estimated from representative filaments and expressed as the range of this population. Where the average filament length was especially great, it was then expressed as greater than the length, which could be accurately measured. For some GFAP mutants, short filaments were indicated by an increase in the number of free filament ends seen in electron micrographs.

Cell culture and transient transfection

Human adrenal cortex carcinoma SW13 (vim-) cells were grown in DMEM supplemented with 10% (vol/vol) fetal calf serum, 2 mM glutamine, 100 U/ml penicillin, and 0.1 mg/ml streptomycin. Cells were maintained in a humidified incubator of 95% (vol/vol) air and 5% (vol/vol) CO_2. Unless otherwise stated, all reagents for cell cultures were purchased from Thermo Fisher Scientific (Waltham, MA). For transient transfection, cells grown on 13-mm coverslips or six-well plates were transfected with the indicated GFAP constructs using the TransIT-LT1 transfection reagent (Mirus Bio, Madison, WI). Cells were processed for immunofluorescence microscopy or extracted for analysis by immunoblotting at 48 h after transfection.

Primary cortical astrocyte cultures and lentiviral transduction

Astrocyte-enriched glial cultures were prepared from embryonic day 18 embryos of Sprague Dawley rats as previously described (Lin *et al.*, 2016). All procedures for animal experiments were approved by the Institutional Animal Care and Use Committee (IACUC) of National Tsinghua University (Approval No. 10912H036). Dissociated cortical astrocytes were plated at a density of 5×10^4 cells/cm^2 onto poly-D-lysine–coated coverslips, plates, or dishes.

Lentiviruses were produced by transiently cotransfecting pLEX vector containing the indicated GFAP constructs with the psPAX2 packaging (#12260; Addgene, Cambridge, MA, St. Louis, MO) and

Antibody	RRID	Host	Epitope	Supplier/reference
Human GFAP	AB_509978	Mouse	a.a. 179–206 of human GFAP	BioLegend
GFAP-α	AB_10672298	Mouse	a.a. 411–422 of human GFAP-α	NeuroMab
GFAP-δ		Rabbit	a.a. 418–431 of human GFAP-δ	This study
GFAP	AB_2532994	Rat	a.a. 119–178 of human GFAP	Thermo Fisher Scientific
GFAP	AB_2631098	Rabbit	Near N395 of human GFAP	Cell Signaling Technology
panGFAP	AB_10013482	Rabbit	Unknown	Dako
GFAP	AB_721051	Mouse	Near N386 of human GFAP	Sigma-Aldrich
αB-crystallin	AB_1659585	Mouse	Bovine αB-crystallin	Enzo Life Sciences
Actin	AB_787885	Mouse	N-terminus of β-actin	Novus
Ubiquitin	AB_331292	Mouse	Full-length bovine ubiquitin	Cell Signaling Technology
Glutamate transporter-1	AB_90949	Guinea pig	C-terminus of rat glutamate transporter-1	Merck Millipore
Connexin 43	AB_94663	Mouse	C-terminus of connexin 43	Merck Millipore

TABLE 3: Summary of antibodies used for immunoblotting and immunostaining.

pMD2.G envelope (#12259; Addgene) vectors at a ratio of 4:3:1 into 293T cells (Thermo Fisher Scientific, Waltham, MA) using the TransIT-LT1 transfection reagent (Mirus Bio, Madison, WI). At 48 h after transfection, culture medium was collected and cleared by centrifugation at 2000 × *g* for 30 min before filtration through a 0.45-μm-pore-size filter. Lentiviruses in the medium were concentrated by Lenti-X concentrator (Takara Bio, Mountain View, CA), aliquoted, and stored at –80°C until use. Lentiviral infection was performed by incubating cells with lentiviruses at a multiplicity of infection (MOI) of 10 in the presence of 8 μg/ml polybrene (Sigma-Aldrich, St. Louis, MO). Under these conditions, approximately 80% of cells were infected as determined by immunofluorescence microscopy. In some experiments, cells infected with empty pLEX-MCS vector were used as a control. Transduced cells were fixed for immunocytochemistry or harvested for biochemical fractionation at the time points indicated in the text.

Immunocytochemistry and confocal microscopy

Cells were fixed in 4% (wt/vol) paraformaldehyde (Electron Microscopy Science, Hatfield, PA) in phosphate-buffered saline (PBS) and permeabilized with 0.2% (wt/vol) Triton X-100 (Sigma-Aldrich, St. Louis, MO) in PBS for 10 min. After blocking with 10% (vol/vol) normal goat serum (Jackson ImmunoResearch Laboratories, West Grove, PA) in PBS for at least 1 h, cells were incubated with specific primary antibody (Table 3) at room temperature for 1 h, followed by staining with Alexa Fluor 488- or 594–conjugated secondary antibodies (Thermo Fisher Scientific, Waltham, MA) at room temperature for 1 h. Nuclei were visualized by staining with 4,6-diamino-2-phenylindole (DAPI). After immunostaining, cells were visualized by a Zeiss LSM800 laser scanning confocal microscope (Carl Zeiss, Jena, Germany) using a 20× (0.7 NA) or 40× (1.3 NA) Apochromat objective lens. Images were acquired at a resolution of 1024 × 1024 pixels and analyzed by the Zen software (Ver. 2.3) taking 0.5 μm optical sections and processed for figures using Adobe Photoshop CC (Adobe Systems, San Jose, CA). At least 10 visual fields were photographed, each corresponding to ~10–50 cells, depending on the magnification. Immunofluorescence images shown are representative of the staining observed in the total cell population. For quantification of GFAP aggregates, several random fields from at least three coverslips were analyzed by visual assessment of the percentage of transduced cells that displayed GFAP-positive accumulation.

Cell fractionation and immunoblotting

Primary astrocytes transduced with either WT or mutant GFAP were rinsed twice with PBS and then homogenized in RIPA lysis buffer (20 mM Tris-HCl, pH 7.4, 5 mM EDTA, 1 mM EGTA (ethylenediaminetetraacetic acid), 150 mM NaCl, 1% [vol/vol] Triton X-100, 0.5% [wt/vol] sodium deoxycholate, and 0.1% [wt/vol] SDS). A cocktail of protease inhibitors (10 μM ALLN, 2 μM leupeptin, 5 μM aprotinin, and 2 mM PMSF, all from Sigma-Aldrich, St. Louis, MO) was added fresh in all buffers before use. A small aliquot of total cell extract was kept aside to analyze total protein contents, and the rest was centrifuged at 17,000 × *g* for 15 min at 4°C. The resulting supernatant was taken as the RIPA-soluble fractions, and the pellets, representing the RIPA-insoluble fraction, were sonicated for 30 s in 1% (wt/vol) SDS buffered with 10 mM Tris-HCl, pH 8, and 5 mM EDTA. Membrane-enriched fractions were prepared from astrocytes by homogenization on ice with a 1 ml Dounce homogenizer in 10 volumes of homogenization buffer (7.5 mM sodium phosphate [pH 7.0], 0.25 M sucrose, 5 mM EDTA, and 5 mM EGTA) containing a cocktail of protease inhibitors. Homogenates were centrifuged at 1000 × *g* in a benchtop centrifuge (Eppendorf; 5415R) for 10 min at 4°C. The supernatants were further centrifuged at 100,000 × *g* in a Micro ultracentrifuge using a S55S rotor (Hitachi HiTech) for 30 min at 4°C, and the resulting pellet was taken as the membrane-enriched fraction. After concentration determination by BCA assay, protein samples were mixed with appropriate volumes of sample buffer (25 mM Tris-HCl, pH 6.8, 10% [vol/vol] glycerol, 1% [wt/vol] SDS, and 5% [vol/vol] β-mercaptoethanol) before immunoblotting analysis.

Protein samples resolved on 12% (wt/vol) or 15% (wt/vol) SDS–PAGE were transferred to nitrocellulose membranes (Pall Life Sciences). Following electrophoretic transfer, membranes were blocked with 3% (wt/vol) BSA in Tris-buffered saline (TBS) with Tween (TBST: 20 mM Tris-HCl, pH 7.4, and 150 mM NaCl, containing 0.1% [vol/vol] Tween 20) at room temperature for at least 1 h. After being washed with TBST three times, membranes were incubated with specific primary antibodies (Table 3) at 4°C overnight, followed by incubation with horseradish peroxidase–conjugated anti-mouse, anti-rabbit, or anti-rat secondary antibodies (Jackson ImmunoResearch, West Grove, PA) at room temperature for at least 1 h. Blots were developed by Enhanced Chemiluminescence substrate (Western Lightning, PerkinElmer Life Sciences, Waltham, MA) and digitized using a LAS 4000 Imaging Analyzer (GE Healthcare). For quantification of GFAP, densitometric analysis was performed on blots

from at least three independent experiments using the ImageQuant software (Ver. 7.0, GE Healthcare, Chicago, IL).

Biochemical fractionation of human brain tissues

Post mortem brain tissues from patients with AxD and non-AxD controls were obtained from the NeuroBioBank Brain and Tissue Repositories; some of them had been used in a previous study (Battaglia *et al.*, 2019). Clinical and genetic details of human brain tissues used in this study are presented in Table 1. Brain tissues (~25 mg) were Dounce homogenized with 1 ml Triton buffer (20 mM Tris-HCl, pH 7.4, 140 mM NaCl, 5 mM EDTA, and 1% [vol/vol] Triton X-100). All buffers were supplemented with a cocktail of protease inhibitors as described above. Lysates were centrifuged at 17,000 × *g* for 10 min at 4°C, and the supernatant was taken as the Triton-soluble fraction. Pellets were further extracted by homogenization with 1 ml of high-salt (HS) buffer (20 mM Tris-HCl, pH 7.4, 140 mM NaCl, 5 mM EDTA, 0.5% [vol/vol] Triton X-100, and 1.5 M KCl) and nutated at 4°C for 1 h. The HS extracts were centrifuged at 80,000 × *g* for 30 min at 4°C, and the supernatant was taken as the HS-soluble fraction. The resulting pellets were further extracted with Triton buffer containing 30% (wt/vol) sucrose followed by the same centrifugation conditions as above to float myelin. The final pellets were resuspended in urea buffer (6 M urea containing 20 mM Tris-HCl, pH 7.4, 5 mM EDTA) and extracted by rotation at 4°C overnight. The urea extracts were centrifuged at 17,000 × *g* for 5 min, and the resulting supernatant was collected as urea-soluble fraction. The urea-insoluble fraction in the pellet, designated as the RF fraction, was resuspended in 1% (wt/vol) SDS buffered by 10 mM Tris-HCl, pH 8, and 5 mM EDTA and sonicated for 30 s. After protein concentration determination by BCA assay, the urea-soluble and RF fractions were diluted with appropriate volumes of sample buffer and then heated at 70°C for 5 min before analysis by immunoblotting.

Generation of GFAP isoform–specific antibodies

Mouse monoclonal anti–GFAP-α antibody was produced recombinantly by transfecting R-mAb expression plasmid (Addgene; plasmid #114536) that coexpresses light and heavy chains driven by two cytomegalovirus promoters (Andrews *et al.*, 2019) into 293T cells using the TransIT-LT1 transfection reagent (Mirus Bio, Madison, WI). The immunogen for this antibody was a peptide dodecamer located at the tail domain of GFAP-α. At 72 h posttransfection, cell culture supernatants were collected, filtered through a 0.45-µm filter (Pall Corporation, Port Washington, NY), and concentrated by centrifugal concentrators (Millipore). To produce antibodies that specifically recognize GFAP-δ, a peptide dodecamer HQIVNGTPPARG that is unique to the human GFAP-δ was synthesized, coupled to keyhole limpet hemocyanin, and used as an immunogen for immunization (Yao-Hong Biotechnology, Taipei, Taiwan). The rabbit serum providing the highest titer and specificity for a predesigned antigen was subsequently used. The isoform-specific antiserum was further purified by affinity chromatography as previously described (Chen *et al.*, 2013). Briefly, CnBr-activated Sepharose 4B beads (GE Healthcare) were resuspended in 1 mM HCl for 30 min. After being washed twice with coupling buffer (0.1 M sodium carbonate, pH 8.3), swelled beads were mixed with 10 mg of immunogen peptide and rotated at 4°C for approximately 16 h. The beads were washed with coupling buffer and blocked in 1 M glycine, pH 8, for 2 h at 4°C. Rabbit antiserum was then loaded onto the peptide column, from which the antigen-specific antibody was eluted with 0.1 M glycine (pH 2.5) into tubes containing 1 M Tris-HCl (pH 9.3).

Statistical analysis

All quantitative measurements were presented as mean ± SD (SD). Two-tailed unpaired *t* tests were used for comparison between control and experiment groups. For all statistical analyses, the data were considered statistically different if $p < 0.05$.

ACKNOWLEDGMENTS

This work was supported by grants from the Ministry of Science and Technology (110-2320-B-007-002, 109-2320-B-007-002, and 108-2918-I-007-013 to M.-D.P.) and National Tsing Hua University (109A2008V6 and 108A0117V6 to N.S.L., A.-W.Y., and M.-D.P.). We thank the BioTEM and the Confocal Imaging Cores in National Tsing Hua University (MOST-104-2731-M-007-002) for the support of this study. We thank the patients and their families for donating their tissues that enabled this study. We also thank the editor and reviewers for their valuable input and constructive suggestions.

REFERENCES

Andrews NP, Boeckman JX, Manning CF, Nguyen JT, Bechtold H, Dumitras C, Gong B, Nguyen K, van der List D, Murray KD, *et al.* (2019). A toolbox of IgG subclass-switched recombinant monoclonal antibodies for enhanced multiplex immunolabeling of brain. eLife 8, e43322.

Bar H, Mucke N, Kostareva A, Sjoberg G, Aebi U, Herrmann H (2005). Severe muscle disease-causing desmin mutations interfere with in vitro filament assembly at distinct stages. Proc Natl Acad Sci USA 102, 15099–15104.

Barlow DJ, Thornton JM (1988). Helix geometry in proteins. J Mol Biol 201, 601–619.

Bassuk AG, Joshi A, Burton BK, Larsen MB, Burrowes DM, Stack C (2003). Alexander disease with serial MRS and a new mutation in the glial fibrillary acidic protein gene. Neurology 61, 1014–1015.

Battaglia RA, Beltran AS, Delic S, Dumitru R, Robinson JA, Kabiraj P, Herring LE, Madden VJ, Ravinder N, Willems E, *et al.* (2019). Site-specific phosphorylation and caspase cleavage of GFAP are new markers of Alexander disease severity. eLife 8, e47789.

Bornheim R, Muller M, Reuter U, Herrmann H, Bussow H, Magin TM (2008). A dominant vimentin mutant upregulates Hsp70 and the activity of the ubiquitin-proteasome system, and causes posterior cataracts in transgenic mice. J Cell Sci 121, 3737–3746.

Brenner M, Goldman JE, Quinlan RA, Messing A (2008). Alexander disease: a genetic disorder of astrocytes. In: Astrocytes in Pathophysiology of the Nervous System, ed. VH Parpura and PG Haydon, Boston, MA: Springer, 591–648.

Chen MH, Hagemann TL, Quinlan RA, Messing A, Perng MD (2013). Caspase cleavage of GFAP produces an assembly-compromised proteolytic fragment that promotes filament aggregation. ASN Neuro 5, e00125.

Chen YS, Lim SC, Chen MH, Quinlan RA, Perng MD (2011). Alexander disease causing mutations in the C-terminal domain of GFAP are deleterious both to assembly and network formation with the potential to both activate caspase 3 and decrease cell viability. Exp Cell Res 317, 2252–2266.

Chernyatina AA, Guzenko D, Strelkov SV (2015). Intermediate filament structure: the bottom-up approach. Curr Opin Cell Biol 32, 65–72.

Cogne B, Bouameur JE, Hayot G, Latypova X, Pattabiraman S, Caillaud A, Si-Tayeb K, Besnard T, Kury S, Chariau C, *et al.* (2020). A dominant vimentin variant causes a rare syndrome with premature aging. Eur J Hum Genet 28, 1218–1230.

Flint D, Li R, Webster LS, Naidu S, Kolodny E, Percy A, van der Knaap M, Powers JM, Mantovani JF, Ekstein J, *et al.* (2012). Splice site, frameshift, and chimeric GFAP mutations in Alexander disease. Hum Mutat 33, 1141–1148.

Fuchs E (1996). The cytoskeleton and disease: genetic disorders of intermediate filaments. Annu Rev Genet 30, 197–231.

Gass JK, Wilson NJ, Smith FJ, Lane EB, McLean WH, Rytina E, Salvary I, Burrows NP (2009). Steatocystoma multiplex, oligodontia and partial persistent primary dentition associated with a novel keratin 17 mutation. Br J Dermatol 161, 1396–1398.

Goldman JE, Corbin E (1991). Rosenthal fibers contain ubiquitinated alpha B-crystallin. Am J Pathol 139, 933–938.

Gromiha MM, Parry DA (2004). Characteristic features of amino acid residues in coiled-coil protein structures. Biophys Chem 111, 95–103.

Gruber M, Lupas AN (2003). Historical review: another 50th anniversary–new periodicities in coiled coils. Trends Biochem Sci 28, 679–685.
Hagemann TL, Gaeta SA, Smith MA, Johnson DA, Johnson JA, Messing A (2005). Gene expression analysis in mice with elevated glial fibrillary acidic protein and Rosenthal fibers reveals a stress response followed by glial activation and neuronal dysfunction. Hum Mol Genet 14, 2443–2458.
Heaven MR, Flint D, Randall SM, Sosunov AA, Wilson L, Barnes S, Goldman JE, Muddiman DC, Brenner M (2016). Composition of Rosenthal fibers, the protein aggregate hallmark of Alexander disease. J Proteome Res 15, 2265–2282.
Heaven MR, Wilson L, Barnes S, Brenner M (2019). Relative stabilities of wild-type and mutant glial fibrillary acidic protein in patients with Alexander disease. J Biol Chem 294, 15604–15612.
Hedberg KK, Chen LB. (1986). Absence of intermediate filaments in a human adrenal cortex carcinoma-derived cell line. Exp Cell Res 163, 509–517.
Helman G, Takanohashi A, Hagemann TL, Perng MD, Walkiewicz M, Woidill S, Sase S, Cross Z, Du Y, Zhao L, *et al*. (2020). Type II Alexander disease caused by splicing errors and aberrant overexpression of an uncharacterized GFAP isoform. Hum Mutat 41, 1131–1137.
Herrmann H, Aebi U (2004). Intermediate filaments: molecular structure, assembly mechanism, and integration into functionally distinct intracellular Scaffolds. Annu Rev Biochem 73, 749–789.
Herrmann H, Strelkov SV, Feja B, Rogers KR, Brettel M, Lustig A, Haner M, Parry DA, Steinert PM, Burkhard P, Aebi U (2000). The intermediate filament protein consensus motif of helix 2B: its atomic structure and contribution to assembly. J Mol Biol 298, 817–832.
Hess JF, Budamagunta MS, FitzGerald PG, Voss JC (2005). Characterization of structural changes in vimentin bearing an epidermolysis bullosa simplex-like mutation using site-directed spin labeling and electron paramagnetic resonance. J Biol Chem 280, 2141–2146.
Hesse M, Grund C, Herrmann H, Brohl D, Franz T, Omary MB, Magin TM (2007). A mutation of keratin 18 within the coil 1A consensus motif causes widespread keratin aggregation but cell type-restricted lethality in mice. Exp Cell Res 313, 3127–3140.
Ivaska J, Pallari HM, Nevo J, Eriksson JE (2007). Novel functions of vimentin in cell adhesion, migration, and signaling. Exp Cell Res 313, 2050–2062.
Jany PL, Hagemann TL, Messing A (2013). GFAP expression as an indicator of disease severity in mouse models of Alexander disease. ASN Neuro 5, e00109.
Kim B, Kim S, Jin MS (2018). Crystal structure of the human glial fibrillary acidic protein 1B domain. Biochem Biophys Res Commun 503, 2899–2905.
Krieger F, Moglich A, Kiefhaber T (2005). Effect of proline and glycine residues on dynamics and barriers of loop formation in polypeptide chains. J Am Chem Soc 127, 3346–3352.
Lee CH, Kim MS, Li S, Leahy DJ, Coulombe PA (2020). Structure-function analyses of a keratin heterotypic complex identify specific keratin regions involved in intermediate filament assembly. Structure 28, 355–362.e354.
Lee SY, Kim S, Lim Y, Yoon HN, Ku NO (2019). Keratins regulate Hsp70-mediated nuclear localization of p38 mitogen-activated protein kinase. J Cell Sci 132, jcs229534.
Li R, Johnson AB, Salomons G, Goldman JE, Naidu S, Quinlan R, Cree B, Ruyle SZ, Banwell B, D'Hooghe M, *et al*. (2005). Glial fibrillary acidic protein mutations in infantile, juvenile, and adult forms of Alexander disease. Ann Neurol 57, 310–326.
Lin NH, Huang YS, Opal P, Goldman RD, Messing A, Perng MD (2016). The role of gigaxonin in the degradation of the glial-specific intermediate filament protein GFAP. Mol Biol Cell 27, 3980–3990.
Lin NH, Messing A, Perng MD (2017). Characterization of a panel of monoclonal antibodies recognizing specific epitopes on GFAP. PLoS One 12, e0180694.
Lin NH, Yang AW, Chang CH, Perng MD (2021). Elevated GFAP isoform expression promotes protein aggregation and compromises astrocyte function. FASEB J 35, e21614.
Lomakin IB, Hinbest AJ, Ho M, Eldirany SA, Bunick CG (2020). Crystal structure of keratin 1/10(C401A) 2B heterodimer demonstrates a proclivity for the C-terminus of helix 2B to form higher order molecular contacts. Yale J Biol Med 93, 3–17.
Meier M, Padilla GP, Herrmann H, Wedig T, Hergt M, Patel TR, Stetefeld J, Aebi U, Burkhard P (2009). Vimentin coil 1A-A molecular switch involved in the initiation of filament elongation. J Mol Biol 390, 245–261.
Messing A, Brenner M (2020). GFAP at 50. ASN Neuro 12, 1759091420949680.
Morgan AA, Rubenstein E (2013). Proline: the distribution, frequency, positioning, and common functional roles of proline and polyproline sequences in the human proteome. PLoS One 8, e53785.
Nicholl ID, Quinlan RA (1994). Chaperone activity of alpha-crystallins modulates intermediate filament assembly. EMBO J 13, 945–953.
Nicolet S, Herrmann H, Aebi U, Strelkov SV (2010). Atomic structure of vimentin coil 2. J Struct Biol 170, 369–376.
Olabarria M, Putilina M, Riemer EC, Goldman JE (2015). Astrocyte pathology in Alexander disease causes a marked inflammatory environment. Acta Neuropathol 130, 469–486.
Olive M, Armstrong J, Miralles F, Pou A, Fardeau M, Gonzalez L, Martinez F, Fischer D, Martinez Matos JA, Shatunov A, *et al*. (2007). Phenotypic patterns of desminopathy associated with three novel mutations in the desmin gene. Neuromuscul Disord 17, 443–450.
Omary MB, Coulombe PA, McLean WH (2004). Intermediate filament proteins and their associated diseases. N Engl J Med 351, 2087–2100.
Parry DA, Steinert PM (1999). Intermediate filaments: molecular architecture, assembly, dynamics and polymorphism. Q Rev Biophys 32, 99–187.
Perng M, Su M, Wen SF, Li R, Gibbon T, Prescott AR, Brenner M, Quinlan RA (2006). The Alexander disease-causing glial fibrillary acidic protein mutant, R416W, accumulates into Rosenthal fibers by a pathway that involves filament aggregation and the association of alpha B-crystallin and HSP27. Am J Hum Genet 79, 197–213.
Perng MD, Cairns L, van den IP, Prescott A, Hutcheson AM, Quinlan RA (1999). Intermediate filament interactions can be altered by HSP27 and alphaB-crystallin. J Cell Sci 112 (Pt 13), 2099–2112.
Perng MD, Wen SF, Gibbon T, Middeldorp J, Sluijs J, Hol EM, Quinlan RA (2008). Glial fibrillary acidic protein filaments can tolerate the incorporation of assembly-compromised GFAP-delta, but with consequences for filament organization and alphaB-crystallin association. Mol Biol Cell 19, 4521–4533.
Pollard TD, Cooper JA (1982). Methods to characterize actin filament networks. Methods Enzymol 85(Pt B), 211–233.
Premchandar A, Mucke N, Poznanski J, Wedig T, Kaus-Drobek M, Herrmann H, Dadlez M (2016). Structural dynamics of the vimentin coiled-coil contact regions involved in filament assembly as revealed by hydrogen-deuterium exchange. J Biol Chem 291, 24931–24950.
Prust M, Wang J, Morizono H, Messing A, Brenner M, Gordon E, Hartka T, Sokohl A, Schiffmann R, Gordish-Dressman H, *et al*. (2011). GFAP mutations, age at onset, and clinical subtypes in Alexander disease. Neurology 77, 1287–1294.
Rikova K, Guo A, Zeng Q, Possemato A, Yu J, Haack H, Nardone J, Lee K, Reeves C, Li Y, *et al*. (2007). Global survey of phosphotyrosine signaling identifies oncogenic kinases in lung cancer. Cell 131, 1190–1203.
Roelofs RF, Fischer DF, Houtman SH, Sluijs JA, Van Haren W, Van Leeuwen FW, Hol EM (2005). Adult human subventricular, subgranular, and subpial zones contain astrocytes with a specialized intermediate filament cytoskeleton. Glia 52, 289–300.
Schietke R, Brohl D, Wedig T, Mucke N, Herrmann H, Magin TM (2006). Mutations in vimentin disrupt the cytoskeleton in fibroblasts and delay execution of apoptosis. Eur J Cell Biol 85, 1–10.
Sharma S, Conover GM, Elliott JL, Der Perng M, Herrmann H, Quinlan RA (2017). alphaB-crystallin is a sensor for assembly intermediates and for the subunit topology of desmin intermediate filaments. Cell Stress Chaperones 22, 613–626.
Sihag RK, Inagaki M, Yamaguchi T, Shea TB, Pant HC (2007). Role of phosphorylation on the structural dynamics and function of types III and IV intermediate filaments. Exp Cell Res 313, 2098–2109.
Smith TA, Steinert PM, Parry DA (2004). Modeling effects of mutations in coiled-coil structures: case study using epidermolysis bullosa simplex mutations in segment 1a of K5/K14 intermediate filaments. Proteins 55, 1043–1052.
Smith TA, Strelkov SV, Burkhard P, Aebi U, Parry DA (2002). Sequence comparisons of intermediate filament chains: evidence of a unique functional/structural role for coiled-coil segment 1A and linker L1. J Struct Biol 137, 128–145.
Snider NT, Omary MB (2014). Post-translational modifications of intermediate filament proteins: mechanisms and functions. Nat Rev Mol Cell Biol 15, 163–177.
Sosunov AA, McKhann GM 2nd, Goldman JE (2017). The origin of Rosenthal fibers and their contributions to astrocyte pathology in Alexander disease. Acta Neuropathol Commun 5, 27.

Strelkov SV, Herrmann H, Geisler N, Wedig T, Zimbelmann R, Aebi U, Burkhard P (2002). Conserved segments 1A and 2B of the intermediate filament dimer: their atomic structures and role in filament assembly. EMBO J 21, 1255–1266.
Tang G, Perng MD, Wilk S, Quinlan R, Goldman JE (2010). Oligomers of mutant glial fibrillary acidic protein (GFAP) inhibit the proteasome system in Alexander disease astrocytes, and the small heat shock protein alphaB-crystallin reverses the inhibition. J Biol Chem 285, 10527–10537.
Tang G, Xu Z, Goldman JE (2006). Synergistic effects of the SAPK/JNK and the proteasome pathway on glial fibrillary acidic protein (GFAP) accumulation in Alexander disease. J Biol Chem 281, 38634–38643.
Tang G, Yue Z, Talloczy Z, Hagemann T, Cho W, Messing A, Sulzer DL, Goldman JE (2008). Autophagy induced by Alexander disease-mutant GFAP accumulation is regulated by p38/MAPK and mTOR signaling pathways. Hum Mol Genet 17, 1540–1555.
Tian R, Gregor M, Wiche G, Goldman JE (2006). Plectin regulates the organization of glial fibrillary acidic protein in Alexander disease. Am J Pathol 168, 888–897.
Toivola DM, Strnad P, Habtezion A, Omary MB (2010). Intermediate filaments take the heat as stress proteins. Trends Cell Biol 20, 79–91.
Walker AK, Daniels CM, Goldman JE, Trojanowski JQ, Lee VM, Messing A (2014). Astrocytic TDP-43 pathology in Alexander disease. J Neurosci 34, 6448–6458.
Zatloukal K, Stumptner C, Fuchsbichler A, Heid H, Schnoelzer M, Kenner L, Kleinert R, Prinz M, Aguzzi A, Denk H (2002). p62 is a common component of cytoplasmic inclusions in protein aggregation diseases. Am J Pathol 160, 255–263.